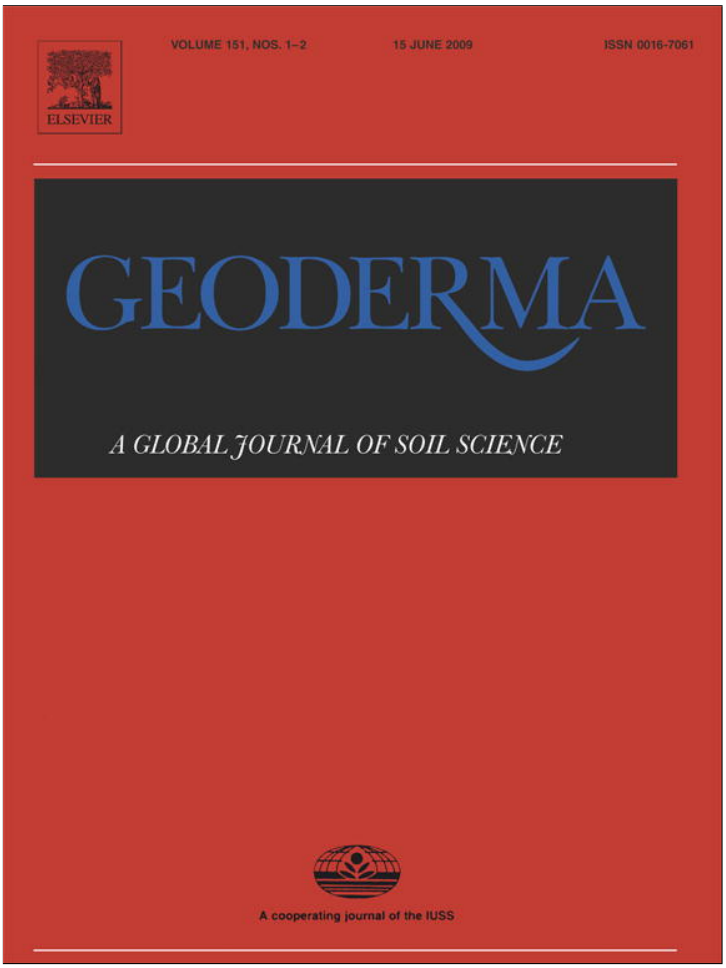

Geoderma 151 (2009) 1–15

Contents lists available at ScienceDirect

Geoderma

journal homepage: www.elsevier.com/locate/geoderma

The temporal evolution of pedogenic Fe–smectite to Fe–kaolin via interstratified kaolin–smectite in a moist tropical soil chronosequence

P.C. Ryan [a,b,*], F.J. Huertas [b,1]

[a] Geology Department, Middlebury College, Middlebury, Vermont, 05753, USA
[b] Departamento de Ciencias de la Tierra y Quimica Ambiental, Estación Experimentál del Zaidín (CSIC), Prof. Albareda 1, 18008 Granada, Spain

ARTICLE INFO

Article history:
Received 23 February 2009
Accepted 13 March 2009
Available online 14 April 2009

Keywords:
Halloysite
Kaolinite
Smectite
Beidellite
Moist tropical soil
Interstratified kaolin–smectite
Costa Rica

ABSTRACT

Fe-rich kaolins in soils of a terrace chronosequence in the moist tropics of Costa Rica are derived from the transformation of smectite via interstratified kaolin–smectite (K–S). The smectite is ferruginous smectite ($10.1 \pm 3.7\%$ Fe_2O_3) that forms early during pedogenesis from basaltic–andesitic parent material and is the dominant mineral in <5 ka soils. Interstratified K–S with 60–90% kaolin layers is the dominant mineral in 10 ka soils, while 125 ka soils contain a physical mixture of Fe–kaolin ($6.0 \pm 1.9\%$ Fe_2O_3) and K–S with >80% kaolin layers.

K–S is indicated by X-ray diffraction (XRD) data that reveal asymmetric 001 peaks between 17.5 and 17.8 Å (ethylene glycol-solvated) and irrational 00*l* peaks that exhibit Méring-like behaviour, and by transmission electron microscopy–analytical electron microscopy (TEM–AEM) data that document single crystals of K–S with compositions intermediate to those of end-member crystals of smectite and kaolin. Lattice fringe images from high resolution TEM (HRTEM) show lateral transitions from smectite layers to kaolin layers via a cell-preserved, layer-by-layer transformation mechanism, and changes in the compositions of tetrahedral and octahedral sheets, notably decreases in octahedral Fe and Mg and tetrahedral Al, indicate that the reaction is accompanied by localized dissolution of smectite 2:1 layers that proceeds laterally. Fourier transform infrared (FTIR) and XRD data indicate that kaolin layers are a mixture of kaolinite and halloysite, and differential thermal analysis–thermogravimetry (DTA–TG) combined with data from XRD and TEM–AEM indicate the development of Al-hydroxy-interlayers in K–S with time.

The soil-forming factors that appear to control formation of K–S are (1) basaltic–andesitic parent that produces high concentrations of base cations and Si in young (<5 ka) soils, and (2) moist tropical climate (3085 mm MAP, 27.3 °C MAT) with a short dry season that fosters formation of smectite in <5 ka soils. By 125 ka, soils are dominated by Fe–kaolin and K–S, helping to constrain reaction rate. The relatively high cation exchange capacity (CEC) of the Fe-rich kaolins (18 ± 12 $cmol_c/kg$) relative to many tropical kaolinites is attributed to small amounts of octahedral Mg and tetrahedral Al inherited from precursor ferruginous smectite layers. Accordingly, the origin (from smectite) and relatively high CEC of the K–S and Fe–kaolin has potentially important implications related to clay mineral reactions and elemental cycling in moist tropical soils.

1. Introduction

The common and generally accurate paradigm for soils of the moist tropics predicts rapid leaching of base cations and Si that results in formation of kaolin very early in soil genesis, in some cases directly from parent materials (e.g. Herbillon, 1980; Nahon, 1991; Quantin et al., 1991). However, kaolin also forms in the humid tropics via transformation from metastable precursor smectite, particularly where base cation concentrations are elevated in poorly-drained areas, deep within soil profiles or in young soils, and often where basaltic parent material is present (Eswaran and de Coninck, 1971; Kantor and Schwertmann, 1974; Ojanuga, 1979; Thanachit et al., 2006).

Typically, the transformation of smectite to kaolin with increasing soil maturity occurs via interstratified K–S (Altschuler et al., 1963; Herbillon et al., 1981; Yerima et al., 1985; Delvaux et al., 1990; Vingiani et al., 2004), yet apparently the K–S pathway has not been documented in the moist tropics—all known occurrences of pedogenic K–S have been documented from Mediterranean, dry tropical, subtropical and temperate climates (Delvaux and Herbillon, 1995) with mean annual precipitation (MAP) generally in the range 500–1500 mm. Yet considering that smectite is known to occur in moist tropical soils (MAP>2000 mm, <three-month dry season) as a metastable precursor to kaolin (Fisher and Ryan, 2006), it is interesting that K–S not been previously documented as an

* Corresponding author. Geology Department, Middlebury College, Middlebury, Vermont, 05753, USA. Tel.: +1 802 443 2557; fax: +1 802 443 2072.
E-mail addresses: pryan@middlebury.edu (P.C. Ryan), javier.huertas@eez.csic.es (F.J. Huertas).
[1] Tel.: +34 958 181600; fax: 34 958 12 96 00.

0016-7061/$ – see front matter © 2009 Elsevier B.V. All rights reserved.
doi:10.1016/j.geoderma.2009.03.010

intermediary in the smectite to kaolin transition in this climate zone. One possible explanation is that smectite dissolves and recrystallizes to form kaolin with no intermediate K–S (Środoń, 1980); however, many investigators (e.g. Hughes et al., 1993; Cuadros et al., 1994; Środoń, 1999) have pointed out that there may be instances where the presence of K–S has gone undetected due to the difficulty of its recognition in routine analyses. Without detailed analysis, K–S can be misidentified as end-member montmorillonite or smectite (in cases of smectite-rich K–S), and halloysite or disordered kaolinite (in cases of kaolin-rich K–S).

Two important considerations regarding the S → K–S → K transformation are reaction rate and consequences for soil exchange chemistry. While the literature contains numerous studies of toposequences containing smectite in cation-rich footslope areas, kaolin in leached upper slope areas, and K–S in intermediate topographic positions (Herbillon et al., 1981; Yerima et al., 1985; Delvaux et al., 1990; Righi et al., 1999), this transition has not yet been observed in a dated sequence that would help to constrain reaction rates. The transition has also been observed in soil profiles, where the S → K–S → K reaction occurs upward from C horizons into upper B horizons with increasing soil development (Churchman et al., 1994), but again, this type of sequence does not lend itself well to examination of reaction rates. Understanding rates and pathways of clay mineral evolution are essential in tropical soils that are dominated by clay minerals, and being able to predict when and where smectite or K–S occur is especially important when considering that they have much higher cation exchange capacities (e.g. 50–100 $cmol_c/kg$) than kaolinite (<10 $cmol_c/kg$) (Churchman et al., 1994).

Nutrient loss from agricultural and silvicultural lands is compounded by the notoriously low CECs of humid tropical soils produced by chemical weathering that ultimately results in a relatively steady-state mineralogical–chemical state characterized by kaolinite and oxyhydroxides of Al and Fe (Birkeland, 1999). These minerals, which form in response to pronounced leaching of Si and base cations (notably, the important plant nutrients Ca and K), yield soils with very low CECs, often <5 $cmol_c/kg$ (Birkeland, 1999). However, in spite of our knowledge of weathering in humid tropical environments, two important issues remain unresolved. The first relates to rates of evolution from freshly deposited (or exposed) parent material toward the nutrient-depleted laterite-Oxisol state—in particular, how rapidly do soils progress from immature, nutrient-rich assemblages to kaolinite–Al–Fe-dominated mature soils? The second pertains to uncertainty regarding to pathways of mineralogical evolution of tropical soils, particularly involving relationships among kaolinite, halloysite, smectite and interstratifications and reactions among these minerals.

Accordingly, the goal of this study is to report the first known occurrence of interstratified K–S in the moist tropics by applying XRD, TEM–AEM, HRTEM, FTIR and DTA–TG to analysis of a soil chronosequence that contains the temporal transition of smectite (ferruginous smectite) to kaolin (Fisher and Ryan, 2006). The specific objectives are to (1) perform analyses designed to ascertain the presence of K–S and (2) study compositions and characteristics of kaolin and smectite layer types in order to examine reaction rates and paragenetic pathways in the transition of smectite to K–S. We also seek to examine the reaction mechanism to determine whether or not the Fe-rich octahedral sheets in ferruginous smectite are preserved during the S → K reaction, as has been observed for the reaction of Al–montmorillonite to kaolinite (Cuadros and Dudek, 2006), and to relate this process to the origin of Fe-bearing kaolinite in the tropics.

2. Study area

The study area is located at the intersection of the Esterillos and Parrita tectonic blocks in the lower Rio Parrita watershed along the central Pacific coast of Costa Rica near the town of Parrita (Sak et al., 2004; Fisher and Ryan, 2006). Soil parent materials are dominated by sediments derived from basalt and andesite mixed with Cretaceous Nicoya Complex ophiolites, predominantly basalt and volcaniclastic sedimentary rock, and the composition of parent material does not appreciably vary among the soils studied (Fisher and Ryan, 2006). Uplift, erosion and deposition has created a series of late Pleistocene and Holocene fluvial fill terraces that, in the field area, are 125 ka (Qt2), 40 ka (Qt3), 10 ka (Qt4) and 5 ka (Qt5) (Sak et al. 2004; Fisher and Ryan, 2006). Fluvial or marine terraces include some of the best examples in the geological record of soil chronosequences (Birkeland, 1999), as they commonly contain information regarding the chronological nature of chemical weathering, including pedogenic mineral paragenesis and element depletion and enrichment trends (Merritts et al., 1992).

Soils in the Esterillos–Parrita area have been mapped at the soil order scale and generally have been classified as Inceptisols with oxic characteristics and affinities toward Oxisols in the oldest soils (Harris et al., 1971; Fisher and Ryan, 2006). Mean annual temperature (MAT) and mean annual precipitation (MAP) for the period extending from 1941–1982 are 27.3 °C and 3085 mm, respectively (Sak et al., 2004). Temperature is relatively constant throughout the year, but precipitation fluctuates seasonally, with a relatively long rainy season marked by maximum monthly precipitation of 570 mm in October, and a relatively short but definite dry season from January to March marked by minimum monthly precipitation of 28.5 mm (in March). This classifies the region as moist tropical, and differentiates it from dry tropical regions with >3 month dry season (where evaporation exceeds precipitation), and wet tropical climates with high rainfall year-round and evaporation<precipitation in all months (Holdridge, 1967). Effectively, the dry tropics produce soils with ustic or xeric moisture regimes, the moist tropics produce soils with udic characteristics and the wet tropics produce perudic soil conditions (Birkeland, 1999). Although widely-applied, the Köppen classification system is not sufficiently detailed to differentiate among tropical sub-climates in areas like Costa Rica, so we are applying the Holdridge system to the climate classification of these soils. Native vegetation in the study area is that of moist tropical forest (Holdridge, 1967), although much of the area has been converted to agriculture (grazing, palm oil plantations).

3. Materials and methods

In a study designed to correlate terraces on the Esterillos and Parrita blocks based on soil mineralogy and geochemistry, Fisher and Ryan (2006) documented the time-dependent transition of pedogenic ferruginous smectite to disordered kaolinite, but they lacked sufficient

Table 1
Details for bulk soil fraction (<2 mm) of samples analyzed in this study, arranged from least-weathered to most-weathered (data from Fisher and Ryan, 2006).

Sample ID	Terrace age	Depth	Color	Bulk soil geochemistry (wt.%)					Bulk soil mineralogy (wt%)						
	(ka)	(cm)	(Munsell)	SiO2	Al2O3	Fe2O3	MgO	CaO	Qtz	Plag	Aug	Goe	Hem	Smec	Kaol
Qt4-C5	10	600	10 YR 7/4	59.58	18.38	12.69	3.48	2.03	8.5	4.2	2.2	<2	<1	85.4	<4
Qt5-B2	5	20	10 YR 3/4	59.38	18.97	13.04	2.52	2.41	12.3	8.9	2.3	6.9	<1	55.9	<4
Qt4-B1	10	10	5 YR 5/6	52.40	23.66	18.53	1.62	0.27	9.7	2.3	<1	8.1	<1	41.4	27.2
Qt4-B3	10	100	2.5 YR 5/6	57.30	27.47	10.62	1.61	0.11	13.2	<0.5	<1	5.9	<1	25.1	32.8
Qt2-B2	125	20	2.5 YR/10R	48.84	27.39	20.14	0.42	0.03	13.4	<0.5	<1	2.9	6.0	<2	68.1

Depth = soil depth sampled, Qtz = quartz, Plag = plagioclase, Aug = augite, Goe = geothite, Hem = hematite, Smec = smectite, Kaol = kaolin.

data to document the presence of K–S as an intermediary phase in the transition of S to K. Thus, specimens selected for the current study (Table 1) span the spectrum of smectite-rich to kaolinite-rich soil and include the <2 μm fraction of four B-horizons (Qt5-B2, Qt4-B1, Qt4-B3, Qt2-B2) and one C-horizon (Qt4-C5). Samples for the current study are from three sites within N 9 34′ ± 2′ and W 84 23′ ± 4′ (Fisher and Ryan, 2006). For the purposes of estimating the age of the deep C-horizon sample Qt4-C5, we have assigned it a value of <5 ka—it contains mineralogical, geochemical and physical characteristics that are less-developed than those of the 5 ka B-horizon sample Qt5-B2, and this age estimate is consistent with the amount of time expected for the weathering front to migrate to a depth of 7 m in a 10 ka terrace deposit.

Note that geochemical and mineralogical data presented in Table 1 are for soil matrix (<2 mm fraction), so, for example, smectite comprises 85% of the <2 mm fraction of soil Qt4-C5 and kaolin comprises 68% of Qt2-B2. Other weathering-related mineralogical and geochemical trends are also evident. Fluvial parent material deposited by the Rio Parrita consists primarily of 12–14% plagioclase, 3–5% augite, 9–12% quartz, 40–50% smectite, 10–20% kaolin. The concentration of smectite increases to 55–85% in <5 ka soils, then decreases to 25–40% in 10 ka B-horizons, and to non-detectable amounts in >40 ka B-horizon soils (Fisher and Ryan, 2006).

All analyses were performed on Ca-saturated clays prepared by suspending 1.0 g of <2 μm fraction in a 20 mL solution of 0.5 M $CaCl_2$, sonifying the suspension to disaggregate clay particles, and it allowing to equilibrate overnight. After centrifuging to separate solids from solution and pouring off supernatant, this process was repeated again with 0.05 and 0.005 M solutions of $CaCl_2$, pouring off supernatant in each case. The resulting Ca-saturated clays were then subsequently washed three times with 40 mL of deionized water to remove any Ca not electrostatically-attracted to mineral particles, and resulting Ca-saturated fractions were used for XRD, HRTEM, FTIR and DTA analyses. Cation exchange capacity (CEC) was estimated from compositions of calcium-saturated individual crystals determined by TEM–AEM analysis, assuming that all calcium in structural formulas occurs in exchange sites (White and Dixon, 2002).

3.1. X-ray diffraction

X-ray diffraction analyses were performed at Estación Experimentál del Zaidín (EEZ) on a PANalytical X'Pert Pro system operating at 45 kV and 40 mA with an X'Celerator detector, CuKα radiation, a Ni filter and 0.25° divergence slit. All analyses were performed on Ca-saturated specimens. Oriented powders were prepared by pipetting concentrated powder suspensions in deionized water onto glass slides, and oriented mounts were continuously scanned from 3–40 °2θ (3.5°/min) in air-dried (AD), ethylene glycol-solvated (EG) and heated (sequentially, 300 °C for 1 h, then 400 °C for 2 h) states. The percentage of kaolin layers in interstratified K–S was calculated by comparing the experimental ethylene–glycol saturated patterns to calculated patterns produced using NEWMOD (Reynolds and Reynolds 1997) and by comparison to data in Cradwick and Wilson (1972) and Moore and Reynolds (1997), with an estimated uncertainty of ±5%. XRD peaks were deconvolved using MacDiff 4.2.5 (Petschick, 2000). Random powder mounts used to examine three-dimensional structures were prepared from gently-ground <2 μm fractions of Ca-saturated powders that were sprinkled onto a zero-background silicon sample holder, cut with a razor blade to enhance random orientation, and coalesced using acetone. These preparations were analyzed from 3–70 °2θ (1.5 °/min) and then from 58–65 °2θ (0.5°/min) to enhance analysis of the 06,33 region.

3.2. Transmission and analytical electron microscopy

Mineralogical textures and compositions were analyzed by TEM–AEM at the Centro de Instrumentación Científica–Universidad de Granada using a Philips CM-20 instrument fitted with an ultrathin window, solid-state Si(Li) detector for energy dispersive X-ray analysis (EDAX). The <2 μm fraction of each specimen was suspended in pure ethyl alcohol and prepared on Cu grids, and analyses were performed at 200 kV with a 200 nm spot size. To image layer spacings, individual crystals of Qt4-B3 were encased in epoxy resin and sliced parallel to the c-axis. Atomic proportions calculated from peak intensities were converted into atomic concentrations using a variety of natural mineral standards and quantitative calibration was carried out by the method of Cliff and Lorimer (1975). The percentage of kaolin layers in interstratified K–S was determined by extrapolation from smectites and kaolin end-member compositions. The high degree of variability in end-member composition, especially smectites, produces an uncertainty of approximately 15%. We are confident that contamination from non-target minerals was minimal. For example, we observed nanometer-size Fe-oxide/hydroxide growths on some smectite, K–S and kaolin crystals, but did not obtain crystal chemistry from these crystals.

3.3. Fourier transform infrared analysis

FTIR spectra were recorded at EEZ on a Perkin-Elmer Spectrum One FTIR spectrometer in absorbance mode (4000 to 400 cm^{-1} range)

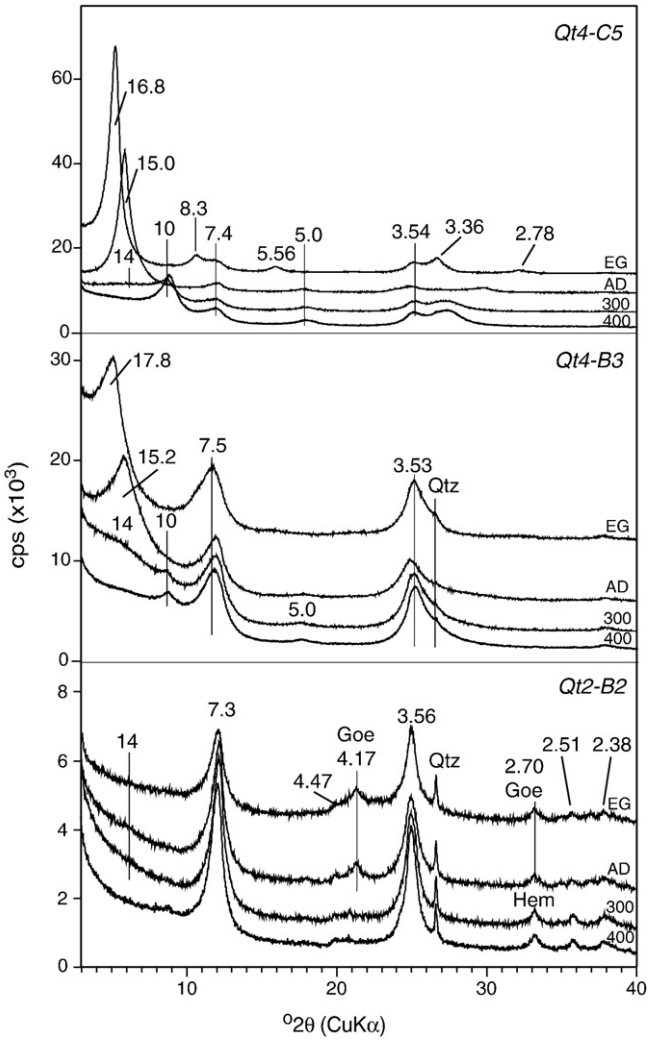

Fig. 1. XRD patterns of oriented mounts of representative specimens in ethylene glycol-solvated (EG), air-dried (AD) and heated to 300 °C (300) and 400 °C (400) states. Peak positions are given in Å. Note differences in intensity (cps) among samples. The presence of hematite is suggested by absence of the goethite 4.17 Å peak in heated Qt2-B2. Samples are arranged from youngest soil (top) to oldest soil (bottom).

with a resolution of 4 cm^{-1}. Samples were prepared in KBr pressed pellets by diluting 1 mg of sample in 150 mg of dried KBr. The pellets were heated overnight at 120 °C before analysis.

3.4. Differential thermal analysis–thermogravimetry

DTA–TG analyses were carried out at EEZ with a Netzsch STA 409EP simultaneous thermal analyzer using 25 mg of sample in an air atmosphere. Al_2O_3 was used as reference material, temperature range was 25 to 1020 °C and heating rate was 10 °C/min. Temperature limits for reactions were determined using the DTA, TG and first derivative of the TG curves (DTG).

4. Results

Data from XRD, TEM–AEM, FTIR and DTA–TG provide evidence for the transition from (1) ferruginous smectite in 5 ka soils, to (2) K–S with 60–90% K layers in 10 ka soils, to (3) Fe-rich kaolin and K–S with 90% K layers in 125 ka soils. Details of data from the four analytical approaches are sequentially presented below, from smectite-rich to interstratified K–S to kaolin-rich specimens.

4.1. Smectite-dominated specimens (Qt5-B2 and Qt4-C5)

4.1.1. XRD analysis

Peak characteristics in oriented XRD mounts (Fig. 1) indicate that these two specimens are dominated by smectite with a symmetrical 001 peak (EG-saturated specimens) at 16.8 Å and higher-order 00*l* peaks at 8.3, 5.56, 4.20, 3.36 and 2.78 Å. Heating to 300 °C causes collapse of the 001 peak to 10 Å with a broad, low-intensity band centered at 14 Å that suggests incomplete collapse of some layers, perhaps due to presence of interlayer Al-hydroxy-interlayers. Further heating to 400 °C caused complete collapse of smectite layers to 10 Å, consistent with dehydroxylation of Al-hydroxy-interlayer complexes (Barnhisel and Bertsch, 1989).The presence of a small amount of kaolin is revealed by the occurrence of peaks at 7.3 and 3.54 Å and the absence of notable shifts in peak position following ethylene glycol solvation or heat treatment. Analysis of randomly-oriented powders (Fig. 2) reveals broad bands typical of smectite, characterized by an 02 band with peak maximum at 4.47 Å and a 06,33 peak with two maxima, one at 1.503 Å that we attribute to ferruginous smectite and one at 1.492 Å produced by kaolin.

Kaolin comprises 10–20% of the <2 mm fraction of modern Rio Parrita sediments (Fisher and Ryan, 2006), suggesting that its

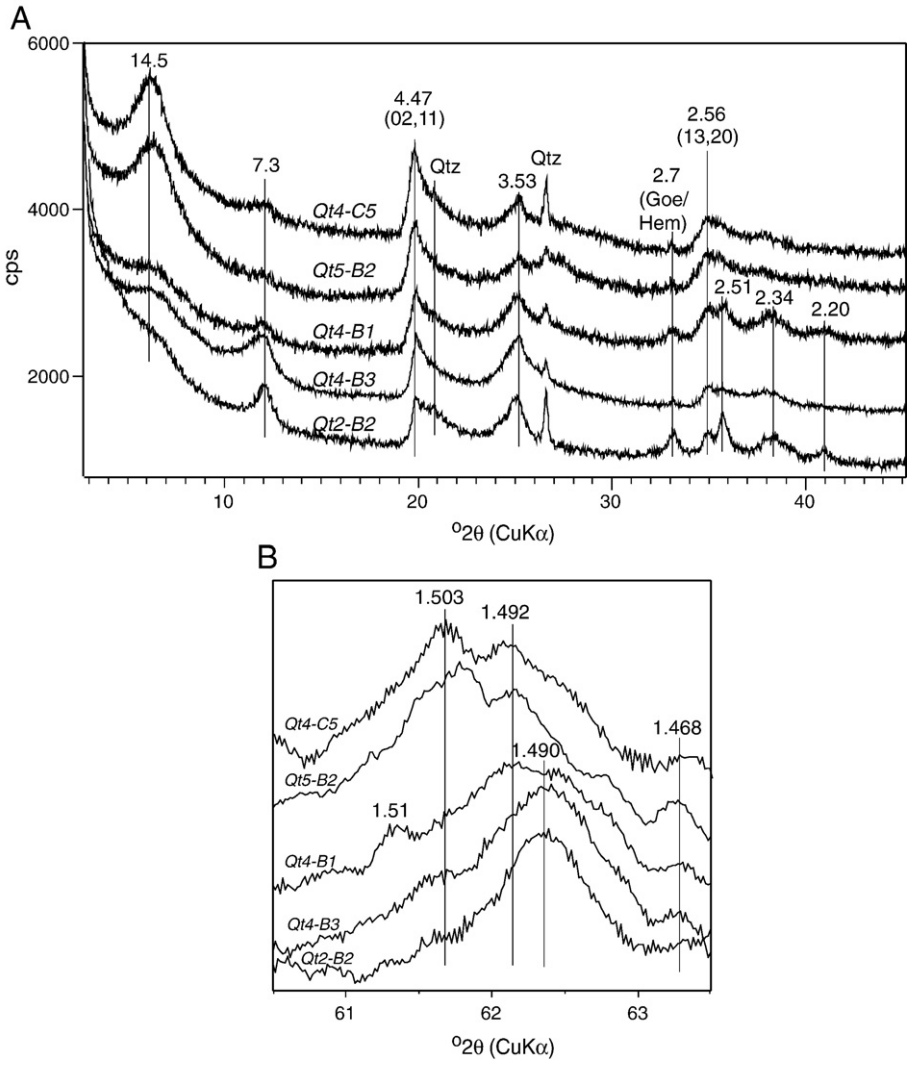

Fig. 2. A. XRD patterns of randomly-oriented mounts. Peak positions are given in Å. Qtz = quartz, Goe = goethite, Hem = hematite. Samples are arranged youngest (Qt4-C5) to oldest (Qt2-B2). B. XRD patterns of 06,33 region from randomly-oriented mounts. Peak positions are given in Å. Nominal end-member smectite (1.503 Å) and kaolin (1.490 Å) spacings are shown.

presence in Qt4-C5 and Qt5-B2 is as relict detrital clay. Evidence for a physical mixture of smectite and kaolin, rather than interstratified K–S, is evident in the separation of the 06,33 region into two peaks, one produced by smectite and one by kaolin (Dudek et al., 2006), and in rational positions of smectite and kaolin 00*l* peaks (Moore and Reynolds, 1997). Small amounts of quartz (4.26 and 3.34 Å) and plagioclase (very weak peaks at 4.04 and 3.2 Å) are also visible in randomly-oriented mounts of these two specimens.

4.1.2. TEM–AEM analysis

Mineral grains in <2 μm fractions are dominated by smectites that occur as individual 0.1–1 μm diameter platy crystals, in some cases with wavy or curled edges. Other pedogenic minerals observed included one crystal each of nontronite and tubular halloysite in Qt4-C5, and one crystal of vermiculite and three crystals of altered biotite with $K_2O > 1.0\%$ in Qt5-B2. Primary augite and plagioclase crystals are rare, but were noted in some views, and oxides of iron were also observed in small amounts (Fig. 3A). The nontronite single crystal (Table 2A) appeared to be crystallizing directly from decomposing augite.

TEM–AEM compositional analysis (Table 2A, B; Fig. 4) indicates that these smectites exhibit notable compositional variability, ranging from relatively Fe–Mg-rich crystals to relatively Al-rich crystals with 0.28 to 0.75 Al atoms per 4 tetrahedral sites (Table 3). The high negative charge derived from the tetrahedral layer is partly compensated by octahedral charges greater than 6.0 mol_c per formula unit (pfu). For example, assuming all Fe is ferric, the Fe–Mg-rich specimens presented in Table 3 possess octahedral charges of +0.13 and +0.44 pfu that partly offset tetrahedral charges of −0.48 and −0.75, and the Al-rich smectite shown in Table 3 contains octahedral charge of +0.30 pfu that partly offsets tetrahedral charge of −0.52 (in this case, producing overall 2:1 layer charge of −0.22).

AEM compositional analysis detects no interstratified kaolin layers in the smectites from Qt4-C5 and Qt5-B2. Compositions are similar to pedogenic ferruginous beidellites from dry tropical soils (Kantor and Schwertman, 1974; Delvaux et al., 1990) and Mediterranean soils (Righi et al., 1998), and the average CEC is 70.4 ± 25 $cmol_c/kg$ (1 SD), similar to values determined by Kantor and Schwertman (1974) from dry tropical soils (~90 $cmol_c/kg$ for the most smectite-rich sample) and by Righi et al. (1998) for beidellites from Mediterranean soils (67–72 $cmol_c/kg$).

Bivariate plots of smectite single crystal compositions determined by AEM are presented in Fig. 5A as wt.% oxide values. The strongest correlation is the inverse relationship between Si and Fe ($R^2 = 0.79$), which may attest to the localized crystallization of smectites with varied composition, controlled by their proximity to the main primary minerals plagioclase and augite. Smectites that crystallize proximal to augites will be Fe-rich and relatively depleted in Si and Al, while those that form proximal to plagioclase will be relatively Al-rich, Si-rich and depleted in Fe and Mg. It is likely for this same reason that Fe and Mg exhibit positive correlation ($R^2 = 0.55$). Given that Si only occurs in

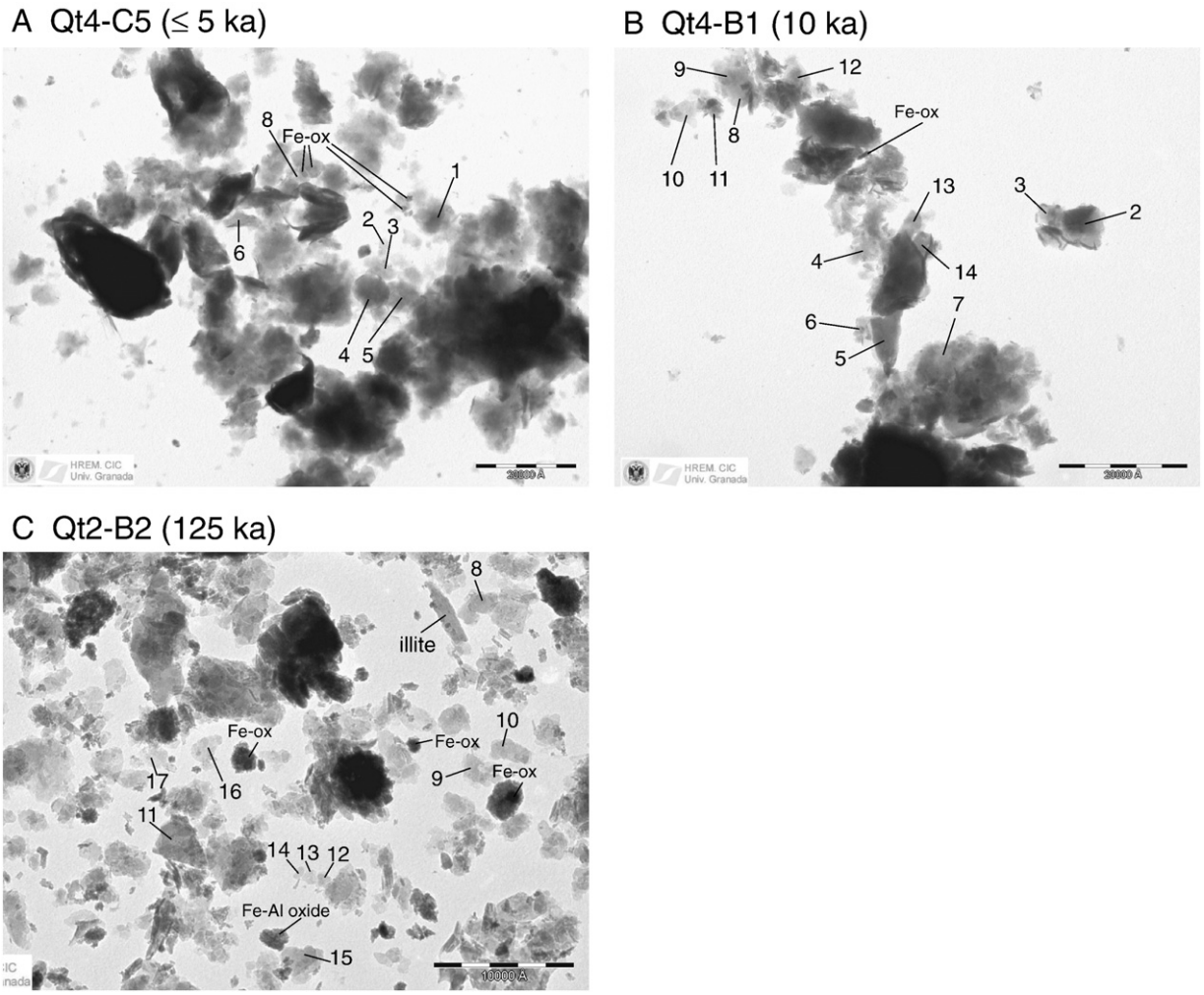

Fig. 3. TEM images of single crystals—note platy morphology with some curled edges. Spot AEM compositional analyses are indicated by numerals and correspond to values in Table 2. Scale bar in A and B is 2 μm; in C it is 1 μm. Qt4-C5: All numbered crystals are smectite. Qt4-B1: 2, 5–10, 12 & 14 are K–S, others are smectite. Qt2-B2: 8, 12–16 are kaolin, others are K–S. Fe-oxides were detected in all samples and are annotated in some cases. The lone illite crystal in Qt2-B2 is likely aeolian in origin.

Table 2
Chemical compositions of single crystals from AEM analyses expressed as wt.% oxide (anhydrous basis), ranging in age from least-evolved soil (Qt4-C5) to most-evolved soil (Qt2-B2).

A. Qt4-C5

	Smectite										Nont	Hall
	1	*2*	*3*	*4*	*5*	*6*	*8*	*10*	*11*	*13*	*12*	*9*
SiO_2	56.04	60.10	67.80	65.67	66.09	66.31	58.18	58.39	61.82	63.10	63.95	52.40
Al_2O_3	25.50	22.86	23.05	26.64	23.61	24.37	31.36	26.83	24.37	27.20	12.09	43.83
Fe_2O_3	11.15	11.44	6.15	5.00	7.15	6.00	7.15	9.29	9.29	7.15	21.01	2.14
MgO	4.48	2.98	1.49	1.33	1.49	2.16	1.66	1.99	2.16	0.99	1.16	0.83
CaO	2.80	2.52	1.40	1.12	1.68	1.26	1.68	3.36	2.38	1.54	1.82	0.84
Na_2O	<0.12	<0.12	<0.12	<0.12	<0.12	<0.12	<0.12	<0.12	<0.12	<0.12	<0.12	<0.12
K_2O	<0.12	<0.12	<0.12	<0.12	<0.12	<0.12	<0.12	<0.12	<0.12	<0.12	<0.12	<0.12
SUM	100.0	99.9	99.9	99.8	100.0	100.1	100.0	99.9	100.0	100.0	100.0	100.0

B. Qt5-B2

	Smectite									K–S	Verm	Altered biotite		
	1	*2*	*3*	*5*	*7*	*9*	*11*	*12*	*13*	*8*	*4*	*6*	*10*	*14*
SiO_2	58.82	60.10	54.12	69.30	49.20	53.47	54.76	54.12	57.97	56.47	58.61	66.74	55.40	57.97
Al_2O_3	25.13	23.43	22.48	22.10	27.02	20.97	27.96	27.02	24.37	35.71	12.66	21.35	22.48	31.55
Fe_2O_3	10.86	10.72	16.87	5.29	17.30	15.73	11.01	11.87	12.29	5.43	8.58	8.29	14.44	6.86
MgO	2.82	2.49	3.32	2.49	4.48	7.13	3.15	4.15	1.99	1.49	18.07	1.16	3.32	1.33
CaO	2.52	2.94	2.52	0.84	1.68	2.52	2.38	2.66	1.82	0.84	2.10	1.26	2.10	0.42
Na_2O	<0.12	<0.12	<0.12	<0.12	<0.12	<0.12	<0.12	<0.12	<0.12	<0.12	<0.12	<0.12	<0.12	<0.12
K_2O	<0.12	0.36	0.72	<0.12	0.48	0.12	0.60	0.24	0.12	<0.12	<0.12	1.08	2.29	1.81
SUM	100.2	100.0	100.0	100.0	100.2	99.9	99.9	100.0	98.6	99.9	100.0	99.9	100.0	99.9

C. Qt4-B1

	Smectite						Kaolin/smectite												
	1	*3*	*4*	*11*	*13*	*18*	*2*	*5*	*6*	*7*	*9*	*8*	*10*	*12*	*14*	*15*	*16*	*17*	*19*
SiO_2	66.84	59.36	63.5	64.08	58.61	64.17	55.83	57.97	58.61	56.72	56.02	53.47	58.56	60.10	57.54	54.33	56.55	60.53	55.76
Al_2O_3	23.73	26.83	25.1	22.67	28.72	28.72	35.71	31.55	34.95	33.38	35.71	34.41	32.53	31.55	33.25	33.63	32.02	30.60	32.15
Fe_2O_3	7.00	9.44	8.15	10.01	8.72	5.43	6.00	8.29	3.43	6.29	6.29	9.29	5.86	6.29	6.43	8.01	8.15	6.00	9.86
MgO	0.99	1.66	1.66	1.49	2.49	0.66	1.99	1.82	0.83	2.82	1.16	0.99	0.99	1.16	2.16	2.82	1.82	0.50	0.99
CaO	1.12	1.40	1.26	1.40	1.12	0.70	0.42	0.42	0.56	0.70	0.42	0.98	1.12	0.70	0.28	0.98	0.98	0.84	0.84
Na_2O	<0.12	<0.12	<0.12	<0.12	<0.12	<0.12	<0.12	<0.12	<0.12	<0.12	<0.12	<0.12	<0.12	<0.12	<0.12	<0.12	<0.12	<0.12	<0.12
K_2O	0.12	1.33	0.24	<0.12	0.36	0.48	<0.12	<0.12	0.72	<0.12	<0.12	0.24	0.48	0.12	<0.12	0.12	0.12	1.08	0.12
SUM	99.8	100.0	100.0	99.7	100.0	100.2	100.0	100.0	99.1	99.9	99.6	99.4	99.6	99.9	99.7	99.9	99.7	99.6	99.7

D. Qt4-B3

	Smectite		Kaolin/smectite														Kaolin			
	2	*20*	*1*	*3*	*4*	*5*	*6*	*7*	*8*	*10*	*13*	*14*	*15*	*17*	*18*	*19*	*9*	*11*	*12*	*21*
SiO_2	63.95	65.88	57.54	60.96	59.04	63.31	62.24	58.39	56.47	55.61	62.50	58.39	62.46	61.82	60.96	63.95	53.69	53.39	54.54	54.33
Al_2O_3	27.39	27.20	38.16	34.19	35.52	32.87	32.68	31.55	35.52	35.89	31.89	37.71	32.87	32.49	34.95	34.76	38.16	40.50	39.43	38.54
Fe_2O_3	5.72	4.57	2.72	2.43	3.43	2.43	3.00	6.72	5.86	5.72	3.29	2.43	3.86	3.72	2.57	0.71	6.72	2.29	4.15	4.57
MgO	1.66	2.16	0.66	0.50	0.5	0.83	0.83	0.66	0.99	2.32	0.66	0.66	0.33	1.33	0.66	0.00	0.99	0.50	0.50	0.83
CaO	0.28	0.28	0.70	0.56	0.42	0.42	0.56	1.12	0.98	0.42	1.12	0.42	0.28	0.28	0.70	0.14	0.28	2.94	0.84	1.40
Na_2O	<0.12	<0.12	<0.12	<0.12	<0.12	<0.12	<0.12	<0.12	<0.12	<0.12	<0.12	<0.12	<0.12	<0.12	<0.12	<0.12	<0.12	<0.12	<0.12	<0.12
K_2O	0.84	<0.12	<0.12	0.24	<0.12	0.12	0.24	1.57	0.12	<0.12	0.12	0.36	0.12	<0.12	<0.12	0.12	<0.12	0.36	0.36	0.36
SUM	99.85	100.1	99.78	98.88	98.90	99.98	99.56	100.0	99.94	99.97	99.58	100.0	99.92	99.63	99.85	99.69	99.84	99.98	99.81	100.0

E. Qt2-B2

	Kaolin									
	1	*6*	*8*	*12*	*13*	*14*	*15*	*16*	*19*	*21*
SiO_2	53.26	51.33	54.76	53.05	49.84	53.26	54.76	49.84	54.33	51.76
Al_2O_3	39.11	37.78	37.22	39.29	40.62	39.48	40.24	42.88	36.46	39.11
Fe_2O_3	7.15	10.29	5.86	3.29	5.72	6.15	3.29	5.15	5.86	7.18
MgO	0.50	0.20	0.83	0.83	2.49	<0.20	1.16	0.83	1.16	0.80
CaO	<0.14	0.53	0.56	2.66	1.12	1.12	0.28	1.40	1.54	0.81
Na_2O	<0.12	<0.12	<0.12	<0.12	<0.12	<0.12	<0.12	<0.12	<0.12	<0.12
K_2O	<0.12	<0.12	0.72	0.84	<0.12	<0.12	0.12	<0.12	0.60	0.35
SUM	100.0	100.1	99.95	99.96	99.78	100.0	99.68	100.1	99.95	100.0

E. Qt2-B2

	Kaolin/smectite															
	2	*3*	*4*	*5*	*7*	*9*	*10*	*11*	*17*	*18*	*20*	*22*	*23*	*24*	*25*	*26*
SiO_2	58.07	56.04	60.96	61.09	55.40	56.90	59.25	56.25	56.25	56.25	62.61	57.22	64.81	63.31	60.75	60.15
Al_2O_3	37.88	40.24	35.14	33.89	41.94	37.97	35.52	32.68	35.89	38.54	34.25	38.58	31.36	31.55	34.95	31.10
Fe_2O_3	3.57	2.14	2.86	3.29	2.57	4.29	4.29	7.86	5.29	2.57	1.72	2.43	2.29	3.72	3.72	6.29
MgO	<0.20	0.99	0.50	0.66	<0.20	0.33	0.50	1.16	1.33	1.33	1.16	0.66	0.99	0.66	0.33	0.99
CaO	<0.14	0.56	0.42	0.56	<0.14	0.42	0.42	0.70	0.98	<0.14	<0.14	0.56	0.42	0.42	0.14	0.84
Na_2O	<0.12	<0.12	<0.12	<0.12	<0.12	<0.12	<0.12	<0.12	<0.12	<0.12	<0.12	<0.12	<0.12	<0.12	<0.12	<0.12
K_2O	<0.12	<0.12	<0.12	<0.12	<0.12	<0.12	<0.12	1.33	<0.12	1.08	<0.12	0.24	<0.12	0.24	0.12	0.60
SUM	99.52	99.98	99.87	99.49	99.91	99.58	99.97	99.98	99.74	99.78	99.73	99.69	99.87	99.90	100.0	100.0

Numbers correspond to individual spot analyses, some of which are shown in Fig. 3. Nont = nontronite, Hall = tubular halloysite, Verm = vermiculite, K–S = kaolin–smectite.

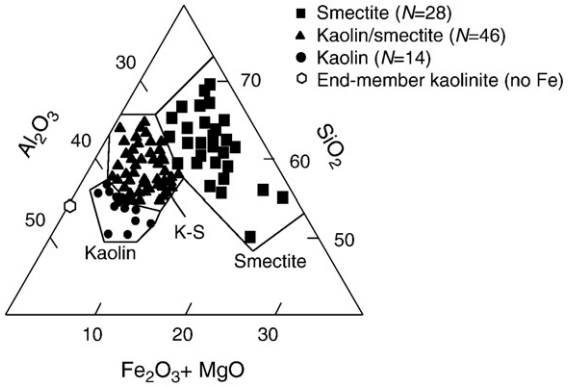

Fig. 4. AEM microanalyses of pedogenic clays (wt.% oxides). Smectites are from <10 ka soils, interstratified kaolin/smectites (K–S) are from 10 and 125 ka soils, and kaolins are mainly from 125 ka soils.

the tetrahedral sheet, lower amounts of Si correspond to higher (more negative) tetrahedral charge, and the inverse correlation between Si and Fe (and also Mg) indicate that the most ferruginous smectites are beidellitic, whereas the smectites with less Fe and Mg are more montmorillonitic. The relatively weak negative correlation between Si and Ca is also attributed to effects of tetrahedral layer charge, where lower amounts of Si produce greater (more negative) tetrahedral layer charge that results in higher exchangeable Ca in interlayers. The lack of correlation between Si and Al, and between Fe and Al, is due to high amounts of Al in both tetrahedral and octahedral sheets.

4.1.3. FTIR analysis

The broad band in FTIR spectra (Fig. 6) at ~3400 cm^{-1} corresponds to OH stretching vibrations of adsorbed water, consistent with predominance of smectite in Qt4-C5 and Qt5-B2, and peaks at 3698 and 3622 cm^{-1} are consistent with XRD and TEM–AEM indications of small amounts of admixed kaolin (Russell and Fraser 1994). The presence of octahedral iron is indicated by the Al–OH–Fe bending band at 870 cm^{-1}, and octahedral Mg is suggested by the weak Al–OH–Mg band at ~840 cm^{-1} (Dudek et al., 2007), consistent with TEM–AEM evidence for Fe_{oct} and Mg_{oct} in Qt4-C5 and Qt5-B2 smectite crystals.

4.1.4. DTA–TG analysis

Two low-temperature endothermic events are indicated by an intense peak at ~100 °C and a smaller peak at ~180 °C (Fig. 7). These peaks correspond to loss of hydration water that is mainly derived from smectite interlayers, released in two stages, the first one corresponding to water that is loosely held by cations (released at ~100 °C) followed by release of water directly coordinated to interlayer cations (~180 °C). Higher temperature reactions (>300 °C) are dominated by weak endothermic peaks at 511–515 °C which correspond to dehydroxylation of kaolin and a broad region of smectite dehydroxylation characterized by weak peaks that show up as dimples on the shoulders of the kaolin peak between 400 and 550 °C (Mackenzie 1970). While aluminous smectites typically exhibit broad dehydroxylation peaks in the 550–650 °C range (Mackenzie, 1970), dehydroxylation at lower temperatures like those seen here has been observed for pedogenic ferruginous smectites from the dry tropics (Kantor and Schwertmann, 1974) and temperate climates (Glassman and Simonson, 1985). The occurrence of octahedral Fe with relatively weak octahedral bonds (409 kJ/mol, respectively) as compared to the Al–O octahedral bond (511 kJ/mol) facilitates dehydroxylation at lower temperature than for typical Al–smectites (Mackenzie, 1970), and trans-vacant smectites (e.g. beidellite and nontronite) have been shown to dehydroxylate at temperatures 150 to 200 °C lower than typical cis-vacant montmorillonites (Drits et al., 1995).

Dehydroxylation weight loss was calculated from TG curves using the inflection point at approximately 350 and the upper limit of 1000 °C, and proportions of smectite and kaolin were estimated from these values using experimental and calculated data for K–S (Dudek et al., 2006). Qt4-C5 exhibited OH loss of 6.17 wt.%, corresponding to the presence of approximately 5–10% kaolin (by wt.), a value that is consistent with TEM, XRD and FTIR observations. Qt5-B2 exhibited dehydroxylation weight loss of 7.73%, suggesting the presence of 10–15% kaolin layers, slightly higher than would be predicted from TEM, XRD and FTIR observations, possibly due to the presence of small amounts of organic matter.

4.2. Intermediate K–S specimens (Qt4-B1 and Qt4-B3)

4.2.1. XRD analysis

Peak positions of specimens in air-dried, ethylene glycol-solvated and heated states indicate the presence of randomly-interstratified K–S in these intermediate-aged samples. Ethylene glycol-solvation produces smectite 001 peaks with notably high *d*-spacings (17.5 to 17.8 Å) and evidence for irrational 00*l* peaks. The high spacing of the 001 peak is characteristic of soil K–S examples in the literature (Bühmann and Grubb, 1991; Righi et al., 1999) and is predicted by calculated patterns (Reynolds and Reynolds, 1997). The positions of the nominal K001 and K002 peaks respond to ethylene glycol solvation in a manner typical of R0 K–S. For example, the broad K001 migrates from 7.35 Å (AD) to 7.55 Å (EG), and the K002 migrates from 3.56 Å (AD) to 3.53 Å (EG). These are typical Méring-type migrations (Méring, 1949) produced by shift of the K001(AD) in the direction of the S002(EG), and the K002(AD) towards the S005(EG). In both cases, peak migrations are produced by shifts in nominal positions of end-member layer types. In the air-dried state, the S002 at 7.5 Å and the K001 at 7.2 Å produce a low-angle shoulder on the 7.35 peak Å. However, in the EG-solvated state, the smectite end-member 002 peak migrates to ~8.4 Å, thus noticeably shifting the apparent K002 towards a lower angle (higher *d*-spacing) and producing a low-angle shoulder. Similarly, the nominal K002(AD) peak contains a low-angle shoulder produced by the S004(AD) peak at 3.75 Å; in the EG state, the end-member S005(EG) peak at 3.36 Å causes migration of the end-member K002 to lower *d*-spacing, and produces a high-angle shoulder. Based on data in Cradwick and Wilson (1972) and Moore and Reynolds (1997), comparison to calculated patterns (Reynolds and Reynolds, 1997) and experimental results (Cuadros et al., 1994), both Qt4-B1 and Qt4-B3 contain kaolin-rich R0 K–S with small amounts of discrete smectite and kaolin. The K–S in Qt4-B1 contains 70% ± 10% K layers, while K–S in Qt4-B3 contains 80% ± 10% K layers.

Peak deconvolution using MacDiff (Petschick, 2000) suggests that the S001(EG) peak for Qt2-B3, for example, is comprised of overlapping components at ~20.3, 18.6 and 16.7 Å; the S002/K001(EG) peak can be deconvolved into overlapping components at 8.4, 7.8, 7.5 and 7.3 Å, and the S005/K002(EG) can be produced by overlapping components at

Table 3
Structural formulas of representative end-member smectites and kaolins from the study area.

Sample	Structural formula	Mineral characteristic
Qt4-C5	$Ca_{0.13}(Al_{1.52}Fe_{0.36}\ Mg_{0.18})(Si_{3.72}Al_{0.28})O_{10}(OH)_2$	Average smectite
Qt5-B2	$Ca_{0.14}(Al_{1.33}Fe_{0.54}\ Mg_{0.30})(Si_{3.48}Al_{0.52})O_{10}(OH)_2$	Average smectite
Qt4-C5	$Ca_{0.17}(Al_{1.30}Fe_{0.51}\ Mg_{0.35})(Si_{3.52}Al_{0.48})O_{10}(OH)_2$	Fe-rich smectite
Qt5-B2	$(Ca_{0.14}K_{0.02})(Al_{1.09}Fe_{0.81}\ Mg_{0.37})(Si_{3.25}Al_{0.75})O_{10}(OH)_2$	Fe-rich smectite
Qt4-C5	$Ca_{0.11}(Al_{1.68}Fe_{0.32}\ Mg_{0.15})(Si_{3.48}Al_{0.52})O_{10}(OH)_2$	Al-rich smectite
Qt2-B2	$Ca_{0.04}(Al_{1.78}Fe_{0.16}\ Mg_{0.05})(Si_{2.0})O_5(OH)_4$	Average kaolin
Qt2-B2	$Ca_{0.05}(Al_{1.82}Fe_{0.15}\ Mg_{0.05})(Si_{1.90}Al_{0.10})O_5(OH)_4$	Al-rich kaolin
Qt2-B2	$Ca_{0.02}(Al_{1.69}Fe_{0.30}\ Mg_{0.01})\ (Si_{1.98}Al_{0.02})O_5(OH)_4$	Fe-rich kaolin

Note that the smectites derive their negative 2:1 layer charge from the tetrahedral sheet and thus are ferruginous beidellites, and also that most of the smectites have slight positive charge in the octahedral sheet.

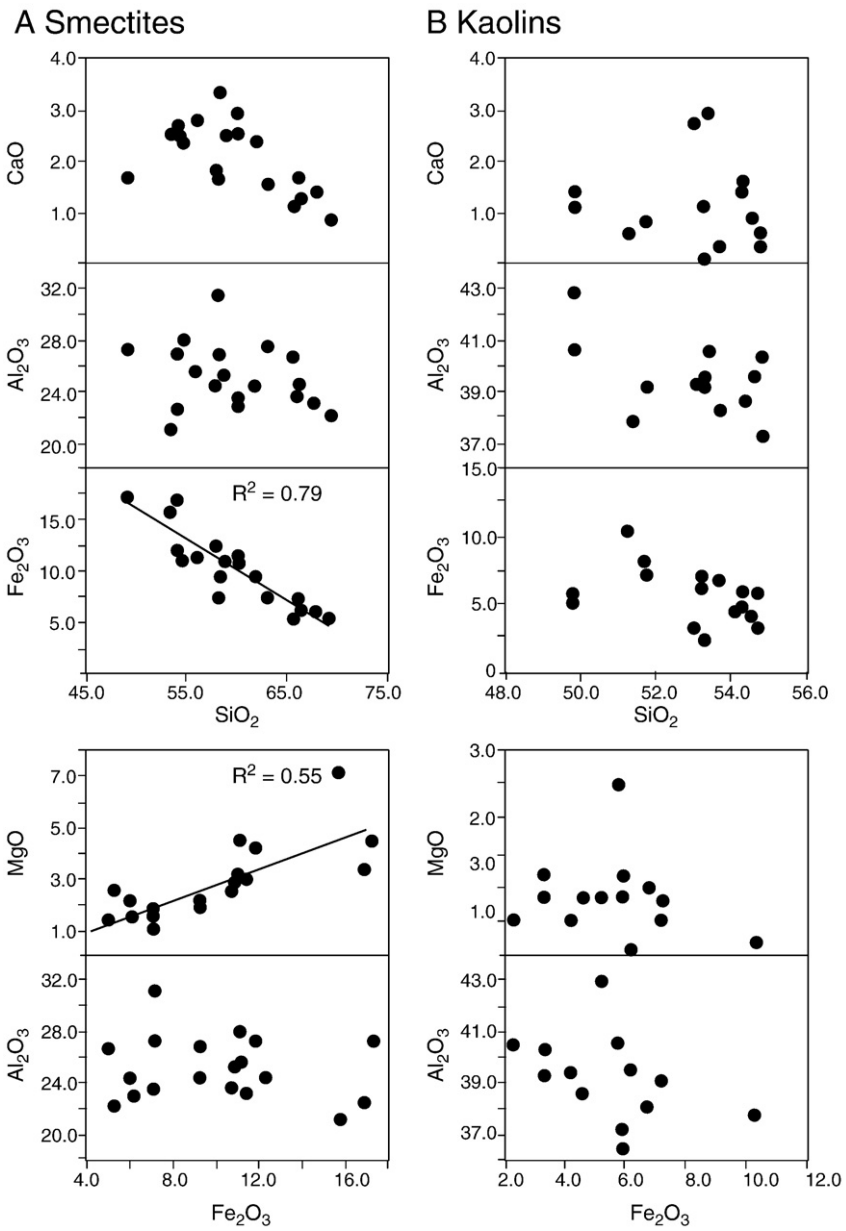

Fig. 5. Bivariate plots of single crystal elemental analyses by AEM for end-member smectites and kaolins. Linear correlations are shown where *R*-squared values are greater than 0.5.

3.57, 3.53 and 3.46 Å. While peak deconvolution likely does not produce a unique solution, it is consistent with a mixture of R0 K–S with a range in the ratio of K:S. For example, a ~20 Å EG peak could be the 002 from a ~40 Å super-order peak produced by packets of KKKS, and a 7.8 Å EG peak could be produced as the 004 from packets of KKS (~31 Å ÷ 4).

Random powder analysis reveals a disordered 02,11 band starting at 4.47 Å and tailing off towards lower *d*-values and a broad 06,33 peak that is centered at ~1.491 Å for Qt4-B1 and 1.490 Å for Qt4-B3 (Fig. 2). In contrast to physical mixtures of kaolin and smectite that produce two distinct peaks or peak maxima in the 06,33 region like those demonstrated by Dudek et al. (2006) and like those present in Qt4-C5 and Qt5-B2, the intermediate samples Qt4-B1 and B3 show only one peak in the 06,33 region that is best explained by K–S that is intimately and randomly interstratified (Dudek et al., 2006).

4.2.2. TEM–AEM and HRTEM analysis

Mineral grains are similar in appearance to those observed in the smectite-dominated samples Qt4-C5 and Qt5-B2, dominated by 0.1–1 μm single crystals, some with curled edges (Fig. 3). No primary silicate minerals were observed, and <0.1 μm crystals of Fe-oxyhydroxide occur as spots on K–S grains or as isolated grains. Accordingly, AEM analyses of K–S grains were conducted in regions lacking Fe oxyhydroxide coatings. The clay crystals in these two specimens contain a range of compositions that are intermediate between end-member smectite and kaolin (Table 2C, D), an observation that is consistent with the presence of K–S crystals of varied K:S ratio. Kaolin-poor crystals contain relatively high SiO_2 (~57–60%) and low Al_2O_3 (32–34%), whereas kaolin-rich K–S crystals contain relatively low % SiO_2 (~53–56%) and high Al_2O_3 (38–41%), and crystals with intermediate K:S are intermediate to these end-members. Values for Fe_2O_3, MgO and exchangeable Ca (as CaO) are similarly distributed, with the highest Fe_2O_3, MgO and CaO values occurring in the most S-rich of the K–S crystals, and decreasing with increasing % K in K–S (Table 2). In general, the K–S crystals are of much more uniform composition than the smectite crystals in WD-C5 and W4-B2, in particular possessing less variability in %SiO_2 (Fig. 4). CEC of the K–S crystals in Qt2-B1 is 22 ± 9 $cmol_c/kg$ and in Qt2-B3 it is 17 ± 11 $cmol_c/kg$ (1 SD).

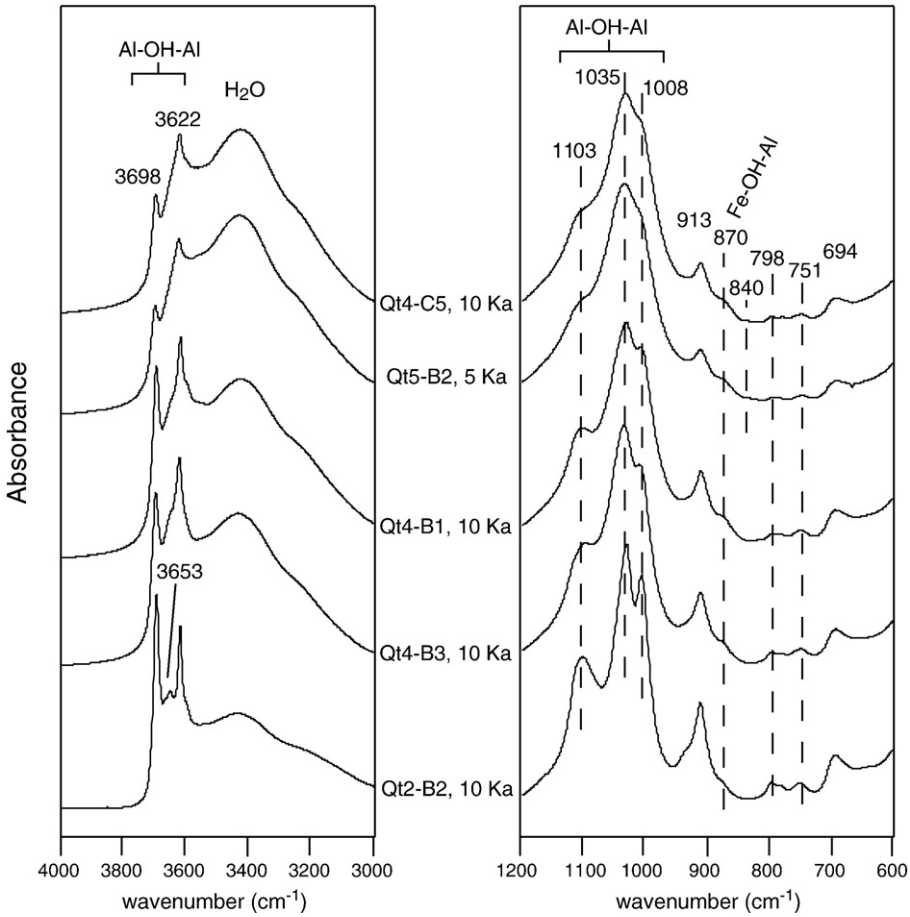

Fig. 6. OH-stretching and OH-bending regions of FTIR spectra, from smectite-rich (top) to kaolin-rich (bottom). Peak positions are in cm^{-1}.

To the best of our knowledge, this is only the third study that has published HRTEM lattice fringe images of K–S (Fig. 8), following those of Churchman et al. (1994) and Amouric and Olives (1998). Such studies are apparently rare because of the difficulty involved in obtaining quality images of the disordered types of interstratified clays that form in weathering environments—white fringes often appear corrugated, exhibit variable thickness and are even absent in some areas, thus complicating interpretation (Veblen et al., 1990; Amouric and Olives, 1998). Nonetheless, HRTEM lattice fringe images from Qt4-B3 (Fig. 8) showed characteristic spacings of randomly interstratified smectite (~13 Å) and kaolin (~7 Å) layer types (Fig. 7). Particularly notable are areas with packets of layers producing the following lattice fringe spacings and stacking arrangements: 13 Å (S), 20 Å (KS), 27 Å (KKS) and ~35 Å (KKKS). Numerous instances of lateral transitions from smectite layers into kaolin layers were also observed, as indicated by arrows on Fig. 8. Lattice-fringe spacings were measured between alternating black and white fringes that were relatively easy to recognize in some regions. However, some areas were more complicated, exhibiting broad white fringes, sometimes with faint gray lines suggesting ~7 Å spacings—we interpret these broad white regions as kaolin-rich zones. The disordered stacking arrangements observed in HRTEM are consistent with XRD data indicating R0 K–S. The 13 Å spacing of smectite layers was also observed by Amouric and Olives (1998), and may reflect the presence of hydroxy-Al interlayers that prevent collapse to 10 Å.

4.2.3. FTIR analysis

The increased intensity of peaks at 3698 and 3622 cm^{-1} and appearance of a peak at 3653 cm^{-1} in the OH-stretching region, and 1103, 1035, 1008, 913 and 694 in the OH-bending region (Fig. 6), are consistent with XRD and TEM–AEM that indicate increasing kaolin content with time. The presence of octahedral iron is indicated by the Al–OH–Fe bending band at 870 cm^{-1}, although it is difficult to say from these FTIR data whether or not the Fe occurs in kaolin layers as well as smectite layers as seen in spectra for Qt4-C5 and Qt5-B2. The broad band in FTIR spectra at ~3400 cm^{-1} is consistent with the presence of smectite layers in K–S indicated by XRD and TEM–AEM.

4.2.4. DTA–TG analysis

The two low-temperature endothermic events at ~100 °C and ~180 °C (Fig. 7) are consistent with presence of smectite layers which, based on XRD and TEM–AEM, predominantly occur in interstratified K–S. The endothermic peak at 516–517 °C is produced by kaolin and this region also contains evidence of weak, broad smectite dehydroxylation peaks in the 400–550 °C range as observed for Qt4-C5 and Qt5-B2. Dehydroxylation weight loss calculated from TG curves indicates loss of 8.74% for Qt4-B1 and 8.91% for Qt4-B3, corresponding to approximately 50–60% kaolin layers in these samples.

4.3. Kaolin-rich specimen (Qt2-B2)

4.3.1. XRD analysis

Peak positions for air-dried, ethylene glycol-solvated and heated states indicate that kaolin is the dominant layer type in this sample. The positions of nominal K001 and K002 peaks at 7.3 and 3.57 Å are virtually unaffected by glycol or heat treatment; however, these treatments do produce changes in low-angle background and relative intensities of K001 and K002 peaks, indicating the presence of expandable layers. Most notable is the change produced by EG-solvation, which causes an increase in the ratio of the K002 relative to

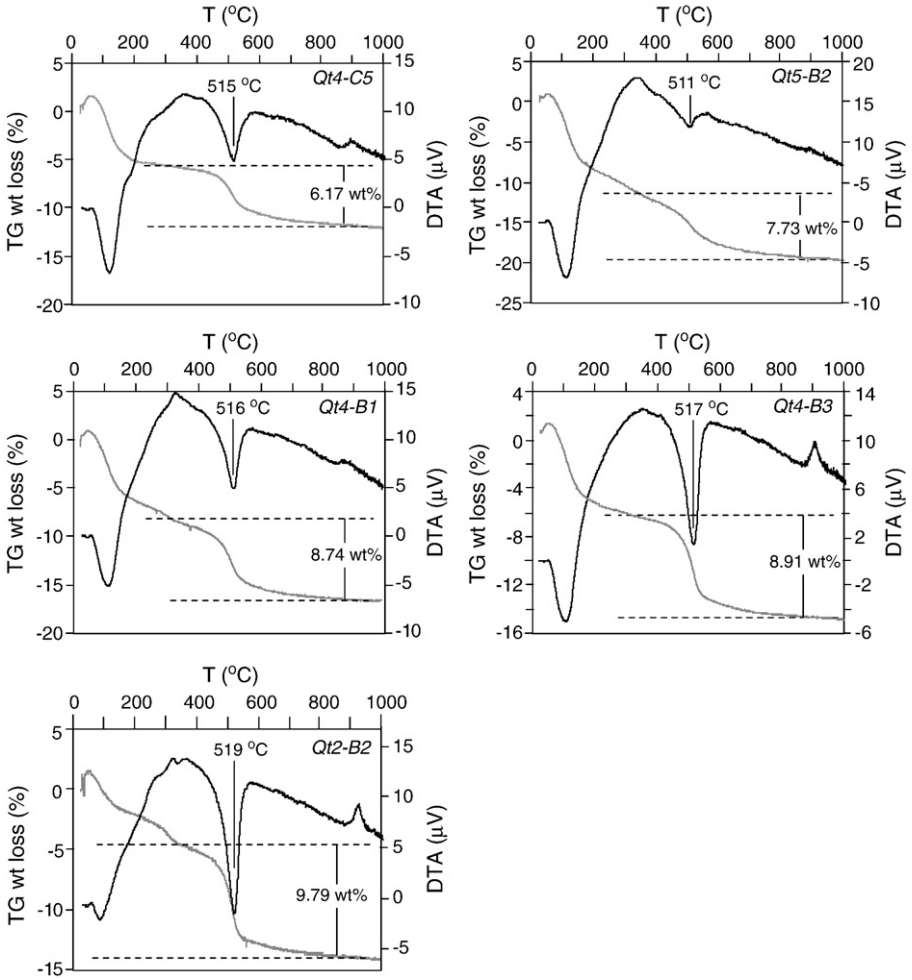

Fig. 7. DTA (black) and TG (gray) curves for smectite-rich (top), intermediate (middle) and kaolin-rich (bottom) samples. Values used to determine % weight loss due to dehydroxylation are shown by dashed lines. Peak dehydroxylation temperatures are also indicated.

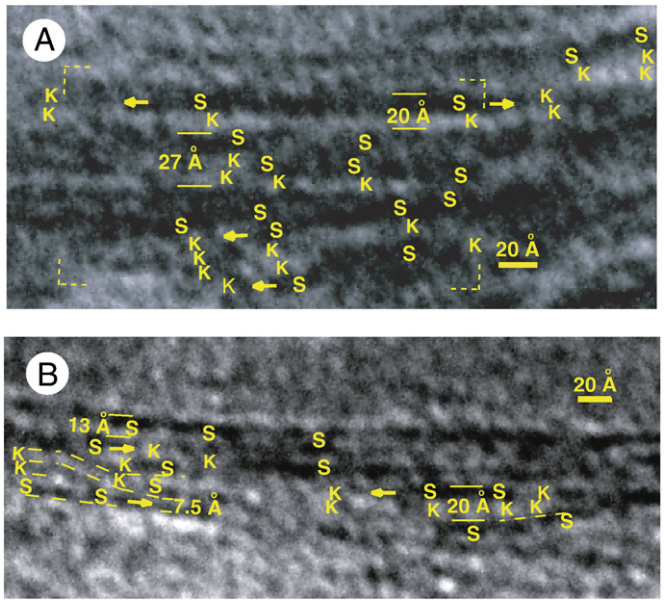

Fig. 8. Lattice fringe images of representative interstratified kaolin–smectites from Qt4-B3, where images A and B represent two separate sub-samples of Qt4-B3. S = smectite layer (~13 Å thick), K = kaolin layer (~7 Å thick). The lateral transition from S to K is indicated by arrows. Note 20 Å spacing for KS packets and 27 Å spacing for KKS packets. Rectangular area denoted by dashed lines in A is reproduced schematically in Fig. 9.

the K001 (as compared to the AD state), behavior that is characteristic of halloysite (MacEwan, 1948; Hillier and Ryan, 2002), where adjacent kaolin layers intercalate glycol to produce a ~10.8 Å *d*-spacing (7.2 + 3.6 Å), the third order of which occurs at 3.6 Å, effectively coincident with the K002. The greater the incidence of expanding kaolin interlayers, the greater the effect. The observation of a single tubular halloysite grain out of the hundreds of crystals seen in TEM analyses does not seem sufficient to explain this XRD characteristic; rather, it is more likely that the kaolin layers contain swelling K–K interfaces, a suggestion that is supported by the existence of exchangeable Ca in many of the kaolins documented by TEM–AEM and indicated by previous data (Bailey, 1989; Cuadros and Dudek, 2006).

Upon initial examination, the lack of peak migration from AD to EG and EG to heated states (Fig. 1) might suggest that this sample does not contain expandable smectite layers (Cradwick and Wilson, 1972), for if it did, we would expect Méring-type migrations like those observed in Qt4-B1 and B3, even for K–S with as little as 10% smectite layers (Moore and Reynolds, 1997). However, the lack of peak migration could also reflect small amounts of interstratified smectite layers that have evolved to the point where their interlayers are dominated by Al-hydroxy-interlayer complexes that do not expand in the presence of ethylene glycol (Delvaux et al., 1990). This suggestion is supported by the presence of a weak 14 Å maximum in AD, EG and 300 °C XRD patterns (Fig. 1) that shifts to 10 Å with heating to 400 °C, consistent with dehydroxylation of Al-hydroxy-interlayers (Barnhisel and Bertsch, 1989), and indicating approximately 10% smectite layers in these K–S crystals.

Random powder mounts reveal an 02,11 band with a peak maximum at ~4.47 Å that tails off towards higher *d*-values with no observable kaolin hkl peaks, data which are indicative of a disordered or turbostratic stacking arrangement. The 06,33 region contains a broad 1.490 Å peak with shoulders at 1.493 Å and 1.479 Å (Fig. 2B). If the 1.490 Å peak accurately represents the position of the 060, the b-dimension of the kaolins is 8.94 Å, a spacing that is similar to the b-dimension of Fe-rich halloysite with 14.7 wt.% Fe_2O_3 that formed in altered pumice (Wada and Mizota, 1982). It is, however, lower than the 8.96–8.98 Å b-dimension of synthesized Fe-rich kaolinites with ~20% Fe_2O_3 (Iriarte et al., 2005). As discussed by Rieder et al. (1992), the complexity of the compound 06,33 peak, which is a composite of the 060, 331 and 331 peaks, can introduce error into determination of b-dimensions.

4.3.2. TEM–AEM analysis

Approximately 40% (10 of 26) of the single crystals in Qt2-B2 analyzed by AEM produce compositions typical of Fe-bearing kaolinites (Fig. 4, Table 2E), with an average composition of 52.62% SiO_2, 39.22% Al_2O_3, 5.99% Fe_2O_3 and <1% each MgO, CaO and K_2O. The average sum of octahedral components ($Al_2O_3 + Fe_2O_3 + MgO$) is 46.0%, equal to the 46.0% value for Al_2O_3 in idealized end-member Al–kaolinite (i.e. with only Al in octahedral sites). The compositions of these crystals exhibit relatively low variability as compared to the smectites and K–S crystals from younger soils in this chronosequence (Fig. 4).

The AEM analyses indicate an average unit cell with minimal tetrahedral Al substitution (<0.1 atoms pfu in four of fifteen kaolin crystals, including the four observed in Qt4-B3), and 1.78 Al, 0.16 Fe and 0.04 Mg atoms per octahedral sheet, on an $O_5(OH)_4$ basis. The presence of a small amount of exchangeable Ca (0.02–0.05 atoms pfu) and trace amounts of K^+ (<0.01 atoms pfu) in some crystals is required to compensate for low layer charge caused by substitution of Mg for Al in the octahedral sheet, and less commonly, by Al for Si substitution in the tetrahedral sheet (Bailey, 1989; Cuadros and Dudek, 2006). This low layer charge (−0.05 to −0.1) can be balanced by inclusion of Ca (and in rare cases, small amounts of K^+) in interlayers between 1:1 layers, a suggestion that is consistent with swelling of adjacent kaolin layers (i.e. halloysitic domains) observed in XRD. Fe values of 0.1 to 0.3 atoms pfu are similar to Fe-rich synthesized kaolinites (e.g. Petit and Decarreau, 1990; Iriarte et al., 2005) and Fe-rich halloysites (Wada and Mizota, 1982), but are higher than the upper limit of 4% Fe_2O_3 (0.1 Fe atoms pfu) previously reported from natural soil kaolinites (Herbillon et al., 1976; Hart et al., 2002).

The average value for the CEC of these kaolins as measured by AEM is 18 ± 13 $cmol_c/kg$ (1 SD) with a range of 0 to 45 $cmol_c/kg$. For comparison, Chorover and Sposito (1995) measured very low CEC values of soil kaolinites from moist tropical forest with <5 $cmol_c/kg$, while Pochet et al. (2007) report halloysites from moist tropical soils with CEC from 20–45 $cmol_c/kg$. Factors that contribute to higher CEC of kaolin include octahedral Fe and tetrahedral Al. The high CEC end-members studied herein contain ~0.05 atoms of tetrahedral Al per mole of kaolin in addition to 0.1 atoms of octahedral Fe and 0.05 atoms of octahedral Mg pfu. Layer charge ranges from 0 to 0.1 pfu.

The remaining single crystals (16 of 26) in Qt2-B2 analyzed by AEM contain SiO_2 contents between 55 and 60%, values that are too high to cast into kaolin structural formulas, but rather clearly indicate 5–15% interstratified S layers in K–S, a finding that is consistent with XRD and DTA–TG data indicating the presence of Al-hydroxy-interlayer smectite. These K–S crystals have average CEC of 12 ± 9 $cmol_c/kg$, a lower value than for K–S in younger soils Qt2-B1 and B3 and kaolin in Qt2-B2.

The ternary SiO_2–Al_2O_3–Fe_2O_3 + MgO diagram (Fig. 4) depicts two notable trends. The first is the time-dependent trend that shows progressively less Fe, Mg and Si in the pedogenic clays, from initially Fe–Mg–Si-rich smectites to intermediate K/S and ultimately Al-rich, Fe-bearing kaolinite. The second is the progressive homogenization of compositions, from smectites characterized by extensive scatter to kaolins with relatively little compositional scatter. For purposes of classifying and plotting, K–S and the S and K end-members are most readily separated by Al content: smectite contains 22–32% Al_2O_3; K–S contains 31–40% Al_2O_3, and kaolin contains 38–43% Al_2O_3 (and <55% SiO_2). Fe, Mg and Si contents are highly varied and not as useful in discrimination except in the case of pure kaolin, which cannot exist with >55% SiO_2.

Bivariate plots of kaolin single crystal compositions determined by AEM (Fig. 5B) as wt.% oxide values exhibit poor correlations compared to those seen in smectite (Fig. 5A). Some of this is due to the narrow range in compositional variability in the kaolins as compared to the smectites (Fig. 4). Yet the data also reveal important changes in the relationships among elements that reflect changes to tetrahedral and octahedral compositions that accompany the reaction of smectite layers to kaolin layers. The lack of correlation between Fe and Mg in kaolin, as compared to the positive Fe–Mg correlation in smectite, reflects changing composition of the octahedral sheet. The weak correlation between Fe and Al is produced by the inverse relationship between these octahedral cations, which is observable in the kaolins (but not the smectites) due to the very low amounts of tetrahedral Al in kaolin. A similar relationship may be apparent in the weak inverse correlation between Si and Al that may reflect small amounts of Al substitution for Si in the tetrahedral sheet.

4.3.3. FTIR analysis

Sharp peaks at 3698 and 3622 cm^{-1} in the OH-stretching region indicate a high kaolin content, as do distinctive kaolin peaks in the OH-bending region at 1103, 1035, 1008, 913, 798, 751 and 694 cm^{-1} (Fig. 6). The presence of the 3653 cm^{-1} peak in the OH-stretching region plus the doublet at 1035 and 1008 cm^{-1} suggest the presence of kaolinite layers (Churchman et al., 1994) although Watanabe et al. (1992) show very similar IR spectra of halloysite with similar peaks. The persistence of the OH-bending peak at 870 cm^{-1} indicates the presence of octahedral Fe in this kaolin-rich sample.

4.3.4. DTA–TG analysis

The presence of small amounts of residual smectite layers are indicated by the low-temperature isotherm at ~100 °C, and high amounts of kaolin in this sample are indicated by the strong dehydroxylation reaction at 519 °C (Fig. 7) which is similar to dehydroxylation of disordered Fe-rich kaolin observed in soils (Varajão et al., 2001; Hart et al., 2002) and created in synthesis experiments (Petit and Decarreau, 1990; Iriarte et al., 2005), and also to Fe-poor synthesized kaolins (Fialips et al., 2000). Two other notable endothermic peaks occur between the dehydration range and the silicate dehydroxylation range. The peak at 290 °C is likely produced by dehydroxylation of goethite (observed in XRD analysis; Fig. 1). The 320 °C peak is attributed to dehydroxylation of gibbsite-like Al-hydroxy-interlayer sheets between smectite 2:1 layers (Barnhisel and Bertsch, 1989), a reaction which can occur at a range of temperatures between 250 and 400 °C depending on exchangeable cation and the degree of development of Al-hydroxy-interlayers (Mackenzie, 1970). Gibbsite undergoes dehydroxylation at 320 °C but there is no evidence for gibbsite in XRD analyses (Figs. 1 and 2), nor was it detected by Fisher and Ryan (2006), so dehydroxylation of smectite Al-hydroxy-interlayers is the more likely explanation. Furthermore, the weak 14 Å maximum in XRD patterns disappears between 300 and 400 °C and is replaced by a 10 Å peak, also consistent with dehydroxylation of Al-hydroxy-interlayers (Barnhisel and Bertsch, 1989).

Weight loss of 9.79% during dehydroxylation (325–1000 °C) indicates that this sample contains 70–75% kaolin, a value lower than what would be predicted by XRD or TEM–AEM analysis. However, it is worth noting that anomalously low dehydroxylation

values have been observed elsewhere for disordered kaolins associated with K–S (Schultz et al., 1971), behavior that may be due to the presence of smectite layers unrecognized by XRD, or to the presence of disordered kaolin layers with low OH content (Brindley et al., 1983). The onset of dehydroxylation was selected as 325 °C for this specimen because this value excludes dehydroxylation at ~290 °C and 315–320 °C produced by goethite and Al-hydroxy-interlayers, respectively, but does include dehydroxylation in disordered kaolin that may occur below 400 °C (Dudek et al., 2006). It also coincides with the inflection points in the DTA and TG curves.

5. Discussion

The combined evidence from XRD, TEM–AEM, FTIR and DTA–TG indicates that pedogenic clays from this moist tropical chronosequence undergo a transformation sequence from (1) ferruginous smectite in <5 ka soils, through (2) a physical mixture in 10 ka soils consisting mostly of K–S (with 60–90% K layers) plus lesser amounts of smectite and kaolin, ultimately to (3) a physical mixture in the oldest soils (125 ka) of Fe–kaolin and K–S with 90% kaolin layers. HRTEM images indicate that the S→K transformation occurs in a cell-preserved layer-by-layer manner; however, the partial loss of octahedral iron during S→K indicates that localized dissolution of 2:1 smectite layers accompanies the formation of 1:1 kaolin layers. Details on the reaction mechanism and layer types, controls on formation of K–S in the moist tropics, and consequences for its formation are presented in the following sections.

5.1. The characteristics of end-member smectite and kaolin

5.1.1. Smectite

The ferruginous smectites in <5 ka soils (Qt4-C5 and Qt5-B2) display compositions and structures similar to other smectites (mainly beidellites) from subtropical and tropical soils, including molar Al:Fe ratios from approximately 2:1 to 6:1, small amounts of octahedral Mg, the presence of Al-hydroxy-interlayers, tetrahedrally-derived layer charge and CEC values of 70 ± 25 $cmol_c/kg$ (Kantor and Schwertmann, 1974; Delvaux et al., 1990; Righi et al., 1998). Al-hydroxy-interlayers like those observed in this study have been documented in pedogenic smectite precursors to K–S (Herbillon et al., 1981; Glassman and Simonson, 1985; Yerima et al., 1985; Delvaux et al., 1990), and as interlayers within smectitic 2:1 layers from tropical soils with high activities of dissolved Al in soil waters (Ndayirigije and Delvaux, 2003). The acidic, Al-rich conditions associated with most tropical soils can produce ~14 Å hydroxy-interlayer 2:1 clays variously termed hydroxy-interlayer smectite (HIS), hydroxy-interlayer vermiculite (HIV), dioctahedral vermiculite and dioctahedral chlorite (Karathanasis, 1988; Barnhisel and Bertsch, 1989; Ndayirigije and Delvaux, 2003). Data from the current study suggest that the proportion of Al-hydroxy-interlayers in smectite increases with soil age, as indicated by increased intensity of the 14-Å peak relative to the 10-Å peak (300 °C preparations) in XRD patterns (Fig. 2).

5.1.2. Kaolin

XRD, FTIR and DTA–TG data indicate that kaolin-rich Qt2-2 is dominated by kaolinite layers with lesser amounts of interstratified halloysite and Al-hydroxy-interlayer smectite. As demonstrated in the assessment of reaction mechanisms below, one of the most commonly cited processes for transforming smectite layers to kaolin layers, stripping of a tetrahedral layer, produces adjacent 7-Å layers that expand with EG-solvation, i.e. 7-Å halloysite (MacEwan, 1948; Hillier and Ryan, 2002). Furthermore, previous studies of disordered kaolins derived from the S→K–S→K transformation have documented interlayer exchangeable cations (Cuadros and Dudek, 2006) that occur in association with 10-Å halloysite layers (Delvaux et al., 1990). In this sense, at least some of the kaolin layers produced by the S→K–S transition documented are best referred to as halloysite. Non-swelling kaolinite layers can be produced by the second transformation mechanism outlined below, where inversion of a tetrahedral layer in the presence of Al-hydroxy-interlayers can yield non-swelling kaolin layers.

The apparent coexistence of both halloysite-like and kaolinite-like interfaces between 7-Å layers leads us to believe that the best term for the 7-Å layers formed during the S→K reaction is kaolin, hence the use of the term kaolin–smectite throughout this paper. It is worth noting that some previous studies of K–S indicate that the 1:1 layers are kaolinite (e.g. Yerima et al., 1985; Churchman et al., 1994; Righi et al., 1999; Cuadros and Dudek, 2006; Dudek et al., 2007), while others indicate that the 1:1 layers are halloysite (Glassman and Simonson, 1985; Delvaux et al., 1990; Quantin et al., 1991).

Compositionally, these appear to be the among the most Fe-rich natural soil kaolins documented to date in the literature, with average Fe_2O_3 of 5.5% and a range of 2.3–10.3 wt.% (0.1 to 0.3 Fe atoms pfu). The apparent upper limit for pedogenic kaolinites is 4 wt.% Fe_2O_3 (Hart et al., 2002); however, halloysites with 14.7% and 9.0% Fe_2O_3 have been documented from altered pumice (Wada and Mizota, 1982) and weathered basaltic ashes (Wada and Kakuto, 1985). Given that our data are from AEM analyses of crystals that show no evidence of contamination by Fe-oxyhydroxides, these values appear to be accurate, and their origin via transformation from smectite layers with 5.0 to 17.3 wt.% Fe_2O_3 (mean = 10.1 wt.%) is the apparent source of the high Fe content.

5.2. Reaction mechanism

HRTEM lattice fringe images clearly indicate randomly interstratified K–S with lateral transitions of S layers to K layers that occur within crystals. An interpretation of the lattice fringe image in Fig. 8A is presented in a schematic sketch in Fig. 9, which depicts two types of lateral transitions that form kaolin layers from smectite layers (Fig. 10). Note that both involve dissolution of the precursor 2:1 layer.

The *first mechanism* involves the stripping of a smectite tetrahedral layer to produce a single kaolin layer (Altschuler et al., 1963; Hughes et al., 1993; Dudek et al., 2006). With respect to the current study, leaching of Si from moist tropical soils produces soil solutions with low concentrations of Si_{aq}, a situation that leads to the destabilization of Si-rich 2:1 layers (Delvaux and Herbillon, 1995).

The *second mechanism* involves the lateral transition from packets of SS into KKS as observed by Amouric and Olives (1998). This transition can be produced by simultaneous inversion of a smectite tetrahedral sheet and lateral transition of a smectite interlayer into a kaolin octahedral sheet (Schultz et al., 1971; Brindley et al., 1983). The presence of Al-hydroxy-interlayers in the smectites would likely enhance this type of transition (Wada and Kakuto, 1983). Acidic soil conditions that enhance Al solubility, paired with low concentrations

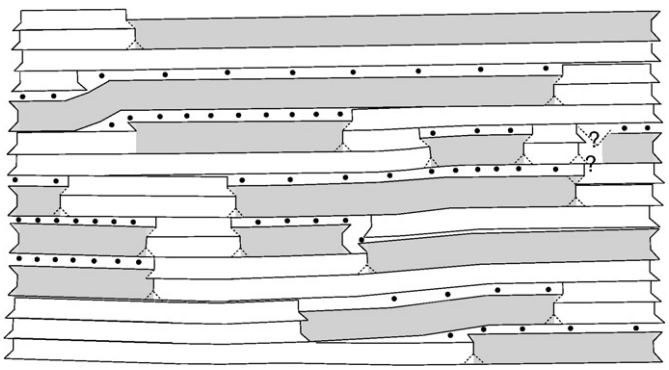

Fig. 9. Interpretation of HRTEM image in Fig. 8A. Smectite layers are gray, kaolin layers are white, and interlayer cations are black circles. Note lateral transitions of smectite layers into kaolin layers by mechanisms that are represented schematically in Fig. 10.

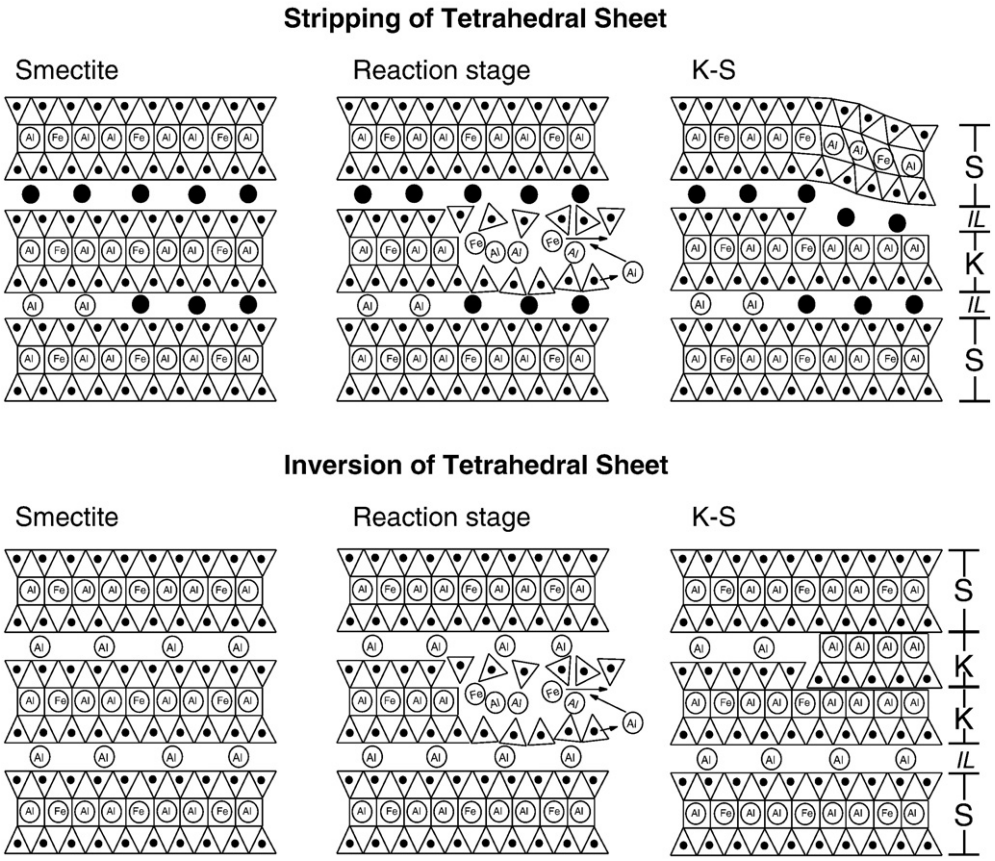

Fig. 10. Potential reaction mechanisms of smectite layers to kaolin layers. In both examples, the octahedral and tetrahedral sheets are shown as dissolving to reflect progressive decreases in octahedral Fe (and Mg) and tetrahedral Al accompanying the S to K transition, as indicated by AEM analyses. Smectite 2:1 layers and kaolin 1:1 layers are denoted by "S" and "K", and expanded interlayers by "IL". Black circles represent cations in interlayer sites; Al atoms in interlayers represent Al-hydroxy-interlayer complexes.

of base cations to occupy interlayers, contributes to the presence of Al-hydroxy-interlayers in smectite, and the lateral transition to a kaolin octahedral sheet from an Al-hydroxy-interlayer appears to be a probable one, as indicated by Wada and Kakuto (1983).

Regardless of the end result, HRTEM and AEM data indicate that the S → K reaction is accompanied by dissolution–precipitation of an S layer within existing cystals of S or K–S (Fig. 10). Evidence for this process is changing composition of octahedral and tetrahedral sheets accompanying the S → K reaction, driven by changes in soil water chemistry that lead to low Si_{aq} and high Al_{aq}, . This type of mechanism has also been proposed by Środoń (1980) and Delvaux et al. (1989), and the Fe liberated by dissolution of smectite octahedral sheets results in formation of pedogenic Fe-oxyhydroxides (Vingiani et al., 2004). The loss of tetrahedral Al accompanying the shift from smectite (0.5 ± 0.2 Al atoms pfu) to kaolin (<0.1 atoms pfu) is also consistent with localized dissolution of 2:1 smectite layers (both tetrahedral sheets and the octahedral sheet). However, it is important to emphasize that lateral transitions observed in lattice fringe images indicate that the reaction occurs in a cell-preserved manner that does not involve dissolution of an entire smectite or K–S *crystal* to form kaolin. Rather, the 2:1 *layers* appear to dissolve progressively in a lateral manner as Al-rich, Si-poor fluids infiltrate crystal edges along interlayers, and the dissolution products are reorganized into kaolin layers that are more Al-rich and Si–Fe-poor than precursor smectite layers. If this is true, tetrahedral stripping and tetrahedral inversion both effectively describe the end-product of the changes to the layer structure that result from dissolution of the smectite 2:1 layer.

Barring extreme distortion of smectite 2:1 layers, tetrahedral stripping necessarily produces expandable K–S interfaces (Fig. 10), including (1) interfaces between tetrahedral sheets of smectite and kaolin and (2) interfaces between a tetrahedral sheet of smectite and an octahedral sheet of kaolin. This type of arrangement has been suggested by Delvaux et al. (1990) and Amouric and Olives (1998), and would result in formation of halloysite. Conversely, tetrahedral inversion does not necessarily produce expandable interfaces between smectite tetrahedral and kaolin octahedral sheets and could result in formation of kaolinite layers.

5.3. Controls on K–S formation in humid tropical soils

The following section considers the fundamental soil forming factors as potential controls on formation of K–S in the moist tropics.

5.3.1. Climate

Mean annual precipitation (MAT) exerts a strong control on K–S formation. Previously documented occurrences of pedogenic K–S occur in Mediterranean (xeric), dry tropical (xeric–ustic) and temperate (ustic) climates with MAP generally between 500 and 2000 mm (Herbillon et al., 1981; Delvaux and Herbillon, 1995; Righi et al., 1999). This appears to be the first documented occurrence of K–S in a moist tropical environment, with 3085 mm MAP and 27.3 °C MAT. The presence of a ~3 month dry season differentiates the central Pacific coast from truly wet tropical climates, including the Atlantic slope of Costa Rica, where there is no dry season and MAP = 4000 mm and MAT is 24 °C. In this climatic regime, soils show no evidence of pedogenic K–S despite the presence of basaltic–andesitic parent material is very similar to parent material in the Esterillos–Parrita region. Pedogenic clays in the Atlantic lowlands are dominated by halloysite and dioctahedral Al-hydroxy-interlayer smectites (Nieuwenhuyse and van Breeman, 1997), even in soils as young as 100–1000 years old (Kautz and Ryan, 2003). Similarly, Holocene soils in Guadaloupe (West Indies) with MAP = 4000 mm and MAT = 22 °C

exhibit a very similar mineralogy and show no evidence of K–S (Ndayiragije and Delvaux, 2003). Thus, the limit of K–S stability appears to lie between moist tropical conditions of 3000 mm MAP with 3-month dry season (favorable) and wet humid tropical conditions characterized by 4000 mm MAP with no dry season (unfavorable).

5.3.2. Organisms

Given that K–S forms across a wide range of climates with varying vegetation types and soil faunal communities, there is no clear evidence that biotic factors exert discernable control on K–S formation. Uptake and recycling of Si and base cations by vegetation in moist tropical forest (Marques et al., 2004) may affect the formation and reaction of K–S, but these relationships are unclear from the data currently available.

5.3.3. Relief/topography

The soils analyzed in this study occur on relatively flat-topped fluvial terraces, so topography is similar for all soils. All soils in the study are well-drained, with no evidence of aquic conditions like those that produce the poorly-drained footslope regions in the numerous red–black toposequences that contain S → K–S → K transitions (e.g. Herbillon et al., 1981; Yerima et al., 1985; Delvaux et al., 1990; Righi et al., 1999).

5.3.4. Parent material

The high concentrations of base cations in basaltic parent material produce conditions favorable for early pedogenic formation of ferruginous smectite that can transform to K–S with leaching of base cations and Si (Delvaux et al., 1990; Delvaux and Herbillon, 1995; Righi et al., 1999). However, the literature contains numerous other examples of soil K–S that form on a wide variety of parent materials, including intermediate to felsic igneous rocks (Watanabe et al., 1992), clastic and carbonate sedimentary rocks (Altschuler et al., 1963; Delvaux and Herbillon, 1995), glacial till and loess (Hughes et al., 1993) and mixed alluvial deposits (Yerima et al., 1985).

5.3.5. Time

Smectites are widely believed to be unstable or metastable precursors to kaolin in tropical soils (Delvaux and Herbillon, 1995; Wilson, 1999), and the data presented herein indicate that ferruginous smectite rapidly transforms to kaolin-rich K–S by 10 ka, and eventually to an assemblage dominated by Fe-rich kaolin by 125 ka. Yet it is interesting to note that K–S persists in 125 ka soils, indicating that that this period of time is insufficient for complete transformation of smectite to kaolin in the moist tropics.

5.4. Potential consequences of K–S and Fe-rich kaolin in moist tropical soils

The soil characteristics most restrictive to plant growth in moist-to-wet tropical forests are low pH, low concentrations of exchangeable Ca and plant-available P, and high amounts of dissolved Al, exchangeable Mn and clay content (Korning et al., 1994). The pronounced leaching of base cations and Si combines to remove mineral-derived plant nutrients (especially Ca and K) while also fostering formation of kaolinite with low CEC (Birkeland, 1999). For this reason, moist-to-wet tropical ecosystems are commonly dominated by highly-weathered, nutrient-depleted Oxisols (Vitousek and Sanford, 1986); however, surficial and crustal processes can produce young land surfaces with relatively high pH, low Al_{aq} and increased nutrient supply compared to typical evolved tropical Oxisols (Porder et al., 2005).

In the moist tropical landscape of the central Pacific coast of Costa Rica, tectonic uplift periodically produces new fluvial (and marine) fill terraces that contain relatively fresh, unweathered fluvial andesitic–basaltic sediment as parent material. With time, these land surfaces evolve from nutrient-rich soils containing smectite and high CEC towards kaolin-rich, oxic soils with lower CEC, resulting in a landscape with soils of varied age and composition. The S → K–S → K transformation sequence observed in this study results in two important consequences for soils of this region, and perhaps other moist tropical regions. The first is that the discrete kaolin crystals contain high cation exchange capacities for kaolin (18 ± 12 $cmol_c/kg$) which may be derived from substitution of small amounts of Mg into octahedral sheets and, in some crystals, Al for Si in tetrahedral sheets. These characteristics are derived from the S → K transformation, where kaolin layers inherit a portion of Mg_{oct}, Al_{tet} (and Fe_{oct}) from precursor Fe-rich smectite layers. Given that clay minerals comprise 50–85% of the reactive fraction (<2 mm) of these soils (Table 1), the presence of smectite-derived Fe–kaolin and K–S is bound to impart higher CECs, and presumably also Ca and K, than might have otherwise be predicted for this ecosystem. Furthermore, the formation of Al-hydroxy-interlayer K–S, as observed in specimens studied herein, has been attributed to lowering concentrations of plant-toxic Al in soil solutions, for example, in moist tropical soils of Ecuador (Korning et al., 1994) and in wet tropical soils of Guadalupe (Ndayiragije and Delvaux, 2003). The absence of gibbsite (and hence free Al) in soils studied herein likely reflects Al uptake by K–S.

The presence of ferruginous smectite in other moist tropical soils (e.g. Eswaran and Deconinck, 1971; Nahon and Colin, 1982) suggests that the S → K–S → K transformation sequence may occur elsewhere in moist tropical ecosystems, and furthermore might indicate that the origin of much of the disordered, Fe-rich kaolin in moist tropical soils is derived from ferruginous smectites. Clearly, these issues warrant further research, particularly given implications for clay mineral origins and elemental cycling in tropical soils.

Acknowledgements

This project was funded by the NSF-Hydrological Sciences (RUI/EAR-0126018), the CSIC-EEZ and Middlebury College. Burch Fisher assisted with field work, Jose Maceira Pena with FTIR and DTA–TG data collection, and Maria del Mar Abad with TEM–AEM imaging and data collection. We also thank M. Vepraskas for editorial handling and S. Petit and an anonymous reviewer for thorough and insightful reviews.

References

Altschuler, Z.S., Dwornik, E.J., Kramer, H., 1963. Transformation of montmorillonite to kaolinite during weathering. Science 141, 148–152.
Amouric, M., Olives, J., 1998. Transformation mechanisms and interstratification in conversion of smectite to kaolinite; an HRTEM study. Clays. Clay. Min. 46, 521–527.
Barnhisel, R.I., Bertsch, P.M., 1989. Chlorites and hydroxy-interlayered vermiculite and smectite, In: Dixon, J.B., Weed, S.B. (Eds.), Minerals in Soil Environments, Second Edition. Soil Sci Soc Am. Madison, Wisconsin, pp. 729–788.
Bailey, S.W., 1989. Halloysite—a critical assessment: proceedings of the International Clay Conference, Strasbourg, France. Scientifique. Geologie. Memoires. 86, 89–98.
Birkeland, P.W., 1999. Soils and Geomorphology, Third Edition. Oxford University Press, New York.
Brindley, G.W., Suzuki, T., Thiry, M., 1983. Interstratified kaolinite–smectites from the Paris Basin; correlations of layer proportions, chemical compositions and other data. Bulletin of Mineralogy 106, 403–410.
Bühmann, C., Grubb, P.L.C., 1991. A kaolin–smectite interstratification sequence from a red and black complex. Clay. Min. 26, 343–358.
Chorover, J., Sposito, G., 1995. Surface charge characteristics of kaolinitic tropical soils. Geochim. Cosmochim. Acta. 59, 875–884.
Churchman, G.J., Slade, P.G., Self, P.G., Janik, L.J., 1994. Nature of interstratified kaolin–smectites in some Australian soils. Australian. J. Soil. Res. 32, 805–822.
Cliff, G., Lorimer, G.W., 1975. The quantitative analysis of thin specimens. J. Microscopy. 103, 203–207.
Cradwick, P.D., Wilson, M.J., 1972. Calculated X-ray diffraction profiles for interstratified kaolinite–montmorillonite. Clay. Min. 9, 395–405.
Cuadros, J., Delgado, A., Cardenete, A., Reyes, E., Linares, J., 1994. Kaolinite/montmorillonite resembles smectite. Clays. Clay. Min. 42, 643–651.
Cuadros, J., Dudek, T., 2006. FTIR investigation of the evolution of the octahedral sheet of kaolinite–smectite with progressive kaolinization. Clays. Clay. Min. 54, 1–11.
Delvaux, B., Herbillon, A.J., 1995. Pathways of mixed-layer kaolin–smectite formation in soils. In: Churchman, G.J., Fitzpatrick, R.W., Eggleton, R.A. (Eds.), Clays Controlling

the Environment: Proceedings of the 10th International Clay Conference, Adelaide, Australia, pp. 457–461.
Delvaux, B., Herbillon, A.J., Vielvoye, L., Mestdagh, M.M., 1990. Surface properties of clay mineralogy of hydrated halloysitic soil clays. II: evidence for the presence of halloysite/smectite (H/Sm) mixed-layer clays. Clay. Min. 25, 141–160.
Delvaux, B., Mestdagh, M.M., Vielvoye, L., Herbillon, A.J., 1989. XRD, IR and ESR study of experimental alteration of Al-nontronite into mixed-layer kaolinite–smectite. Clay. Min. 24, 617–630.
Drits, V.A., Besson, G., Muller, F., 1995. An improved model for structural transformations of heat-treated aluminous dioctahedral 2:1 layer silicates. Clays. Clay. Min. 43, 718–731.
Dudek, T., Cuadros, J., Fiore, S., 2006. Interstratified kaolinite–smectite: nature of the layers and mechanism of smectite kaolinization. Am. Mineral. 91, 159–170.
Dudek, T., Cuadros, J., Huertas, J., 2007. Structure of mixed-layer kaolinite–smectite and smectite-to-kaolinite transformation mechanism from synthesis experiments. Am. Mineral. 92, 179–192.
Eswaran, H., de Coninck, F., 1971. Clay mineral formations and transformations in basaltic soils in tropical environments. Pedologie 21, 181–210.
Fialips, C.-I., Petit, S., Decarreau, A., Beaufort, D., 2000. Influence of synthesis pH on kaolinite "crystallinity" and surface properties. Clays. Clay. Min. 48, 173–184.
Fisher, G.B., Ryan, P.C., 2006. The smectite to disordered kaolinite transition in a tropical soil chronosequence, Pacific Coast, Costa Rica. Clays. Clay. Min. 54, 571–586.
Glassman, J.R., Simonson, G.H., 1985. Alteration of basalt in soils of western Oregon. Soil. Sci. Soc. Am. J. 49, 262–273.
Harris, S.A., Neumann, A.M., Stouse Jr., A.D., 1971. The major soil zones of Costa Rica. Soil. Sci. 112, 439–451.
Hart, R.D., Gilkes, R.J., Siradz, S., Singh, B., 2002. The nature of soil kaolins from Indonesia and western Australia. Clays. Clay. Min. 50, 198–207.
Herbillon, A.J., 1980. Mineralogy of oxisols and oxic materials. In: Theng, B.K.G. (Ed.), Soils with Variable Charge. New Zealand Society of Soil Science, Lower Hutt, New Zealand, pp. 109–126.
Herbillon, A.J., Frankart, R., Vielvoye, L., 1981. An occurrence of interstratified kaolinite–smectite minerals in a red–black soil toposequence. Clay. Min. 16, 195–201.
Herbillon, A.J., Mestdagh, M.M., Vielvoye, L., Derouane, E.G., 1976. Iron in kaolinite with special reference to kaolinite from tropical soils. Clay. Miner. 11, 201–220.
Hillier, S., Ryan, P.C., 2002. Identification of halloysite (7 Å) by ethylene glycol solvation: the 'MacEwan effect'. Clay. Min. 37, 487–496.
Holdridge, L.R., 1967. Life Zone Ecology. Tropical Science Center, San Jose, Costa Rica.
Hughes, R.E., Moore, D.M., Reynolds Jr., R.C., 1993. The nature, detection and occurrence, and origin of kaolinite/smectite. In: Murray, H.H., Bundy, W.M., Harvey, C.C. (Eds.), Kaolin Genesis and Utilization. Special Publication No. 1. Clay Minerals Society, Boulder, Colorado, pp. 291–323.
Iriarte, I., Petit, S., Huertas, F.J., Fiore, S., Grauby, O., Decarreau, A., Linares, J., 2005. Synthesis of kaolinite with a high level of Fe^{3+} for Al substitution. Clays. Clay. Min. 53, 1–10.
Kantor, W., Schwertmann, U., 1974. Mineralogy and genesis of clays in red–black toposequences in Kenya. J. Soil. Sci. 25, 67–78.
Karathanasis, A.D., 1988. Compositional and solubility relationship between aluminum-hydroxy-interlayered soil smectite and vermiculite. Soil. Sci. Soc. Am. J. 52, 1500–1508.
Kautz, C.Q., Ryan, P.C., 2003. The 10 Å to 7 Å halloysite transition in a tropical soil sequence, Costa Rica. Clays. Clay. Min. 51, 252–263.
Korning, J., Thomsen, K., Dalsgaard, K., Nørnberg, P., 1994. Characters of three udults and their relevance to the composition and structure of virgin rain forest of Amazonian Ecuador. Geoderma 63, 145–164.
MacEwan, D.M.C., 1948. Complexes of clays with organic compounds I. Complex formation between montmorillonite and halloysite and certain organic liquids. Trans. Faraday. Soc. 44, 349–367.
Mackenzie, R.C., 1970. Simple phyllosilicates based on gibbsite- and brucite-like sheets. In: Mackenzie, R.C. (Ed.), Differential Thermal Analysis. Academic Press, London, pp. 498–537.
Marques, J.J., Schulze, D.G., Curi, N., Mertzman, S.A., 2004. Major element geochemistry and geomorphic relationships in Brazilian Cerrado soils. Geoderma 119, 179–195.
Méring, J., 1949. L'intereférence des Rayons X dans les systèmes à stratification désordonée. Acta. Crystallographica. 2, 371–377.
Merritts, D.J., Chadwick, O.A., Hendricks, D.M., Brimhall, G.H., Lewis, C.J., 1992. The mass balance of soil evolution on late Quaternary marine terraces, northern California. Geol. Soc. Am. Bull. 104, 1456–1470.
Moore, D.M., Reynolds Jr., R.C., 1997. X-ray Diffraction and the Identification and Analysis of Clay Minerals. Oxford University Press, New York.
Nahon, D.B., 1991. Introduction to the Petrology of Soils and Chemical Weathering. John Wiley and Sons, New York. 313 pp.
Nahon, D.B., Colin, F., 1982. Chemical weathering of orthopyroxenes under lateritic conditions. Am. J. Sci. 282, 1232–1243.
Ndayiragije, S., Delvaux, B., 2003. Coexistence of allophone, gibbsite, kaolinite and hydroxy-Al-interlayered 2:1 clay minerals in a perudic Andosol. Geoderma 117, 203–214.
Nieuwnhuyse, A., van Breemen, N., 1997. Quantitative aspects of weathering and neoformation in selected Costa Rican volcanic soils. Soil. Sci. Soc. Am. J. 61, 1450–1458.
Ojanuga, A.G., 1979. Clay mineralogy of soils in the Nigerian tropical savanna regions. Soil. Sci. Soc. Am. J. 43, 1237–1242.
Petit, S., Decarreau, A., 1990. Hydrothermal (200°C) synthesis and crystalchemi stry of iron-rich kaolinites. Clay. Min. 25, 181–196.
Petschick, R., 2000. MacDiff. http://www.ccp14.ac.uk/ccp/ccp14/ftp-mirror/krumm/Software/macintosh/macdiff/MacDiff.html. Accessed 18 July 2008.
Pochet, G., Van der Velde, M., Vanclooster, M., Delvaux, B., 2007. Hydric properties of high charge, halloysitic clay soils from the tropical South Pacific region. Geoderma 138, 96–109.
Porder, S., Asner, G.P., Vitousek, P.M., 2005. Ground-based and remotely sensed nutrient availability across a tropical landscape. Proc. Nat. Acad. Sci. 102, 10909–10912.
Quantin, P., Balesdent, J., Bouleau, A., Delaune, M., Feller, C., 1991. Premiers stades d'altèration de ponces volcaniques en climat tropical humide (Montagne Pelèe, Martinique). Geoderma 50, 125–148.
Reynolds Jr., R.C., Reynolds III, R.C., 1997. NEWMOD-for-Windows©: A Computer Program for the Calculation of One-dimensional Diffraction Patterns of Mixed-Layered Clays. (published by the authors, Hanover, New Hampshire, USA).
Rieder, M., Guidotti, C.V., Sassi, F.P., Weiss, Z., 1992. Muscovites: d_{060} versus $d_{331\ Å,060}$ spacing: its use for geobarometric purposes. Eur. J. Min. 4, 843–845.
Righi, D., Terribile, F., Petit, S., 1998. Pedogenic formation of high-charge smectite in a vertisol of Sardinia (Italy). Clays. Clay. Min. 46, 167–177.
Righi, D., Terribile, F., Petit, S., 1999. Pedogenic formation of kaolinite–smectite mixed layers in a soil toposequence developed from basaltic parent material in Sardinia (Italy). Clays. Clay. Min. 47, 505–514.
Russell, J.D., Fraser, A.R., 1994. Infrared methods. In: Wilson, M.J. (Ed.), Clay Mineralogy: Spectroscopic and Chemical Determinative Methods. Chapman & Hall, London, pp. 11–67.
Sak, P.B., Fisher, D.M., Gardner, T.W., Murphy, K., Brantley, S.L., 2004. Rates of weathering rind formation on Costa Rican basalt. Geochim. Cosmochim. Acta. 68, 1453–1472.
Schultz, L.G., Shepard, A.O., Blackmon, P.D., Starkey, H.C., 1971. Mixed-layer kaolinite–montmorillonite from theYucatan Peninsula, Mexico. Clays. Clay. Min. 19, 137–150.
Środoń, J., 1980. Synthesis of mixed-layer kaolinite/smectite. Clays. Clay. Min. 26, 419–424.
Środoń, J., 1999. Nature of mixed-layer clays and mechanisms of their formation and alteration. Ann. Rev. Earth. Plan. Sci. 27, 19–53.
Thanachit, S., Suddhiprakarn, A., Kheoruenromne, I., Gilkes, R.J., 2006. The geochemistry of soils on a catena on basalt at Khon Buri, northeast Thailand. Geoderma 135, 81–96.
Varajão, A.F.D.C., Gilkes, R.J., Hart, R.D., 2001. The relationships between kaolinite crystal properties and the origin of materials for a brazilian kaolin deposit. Clays. Clay. Min. 49, 44–59.
Veblen, D.R., Guthrie, G.D., Livi, K.J.T., Reynolds, R.C., 1990. High resolution transmission electron microscopy and electron diffraction of mixed-layer illite/smectite: experimental results. Clays. Clay. Min. 38, 1–13.
Vingiani, S., Righi, D., Petit, S., Terribile, F., 2004. Mixed-layer kaolinite–smectite minerals in a red–black soil sequence from basalt in Sardinia, Italy. Clays. Clay. Min. 52, 473–483.
Vitousek, P.M., Sanford Jr., R.L., 1986. Nutrient cycling in moist tropical forest. Ann. Rev. Ecol. Systematics. 17, 137–167.
Wada, K., Kakuto, Y., 1983. Intergradient vermiculite–kaolin mineral in a Korean ultisol. Clays. Clay. Min. 31, 183–190.
Wada, K., Kakuto, Y., 1985. Embryonic halloysites in Ecuadorian soils derived from volcanic ash. Soil. Sci. Soc. Am. J. 49, 1309–1319.
Wada, S.-I., Mizota, C., 1982. Iron-rich halloysite (10Å) with crumpled lamellar morphology from Hokkaido, Japan. Clays. Clay. Min. 30, 315–317.
Watanabe, T., Sawada, Y., Russell, J.D., McHardy, W.J., Wilson, M.J., 1992. The conversion of montmorillonite to interstratified halloysite–smectite by weathering in the Omi acid clay deposit, Japan. Clay. Min. 27, 159–173.
White, G.N., Dixon, J.B., 2002. Kaolin-serpentine minerals. In: Dixon, J.B., Schulze, D.G. (Eds.), Soil Mineralogy with Environmental Applications. Soil Sci Soc Am. Madison, Wisconsin, pp. 389–414.
Wilson, M.J., 1999. The origin and formation of clay minerals in soils; past, present and future perspectives. Clay. Min. 34, 7–25.
Yerima, B.P.K., Calhoun, F.G., Senkayi, A.L., Dixon, J.B., 1985. Occurrence of interstratified kaolinite–smectite in El Salvador Vertisols. Soil. Sci. Soc. Am. J. 49, 462–466.